

Review

Proton-Conducting Ceramic Membranes for the Production of Hydrogen via Decarbonized Heat: Overview and Prospects

Maria Giovanna Buonomenna 

Ordine Regionale dei Chimici e Fisici della Campania, Via A. Tari 22, 80138 Naples, Italy; mg.buonomenna@chimici.it

Abstract: Proton-conducting ceramic membranes show high hydrogen ion conductivity in the temperature range of 300–700 °C. They are attracting significant attention due to their relevant characteristics compared to both higher-temperature oxygen ion-conducting ceramic membranes and lower-temperature proton-conducting polymers. The aim of this review is to integrate the fundamentals of proton-conducting ceramic membranes with two of their relevant applications, i.e., membrane reactors (PCMRs) for methane steam reforming (SMR) and electrolysis (PCEC). Both applications facilitate the production of pure H₂ in the logic of process intensification via decarbonized heat. Firstly, an overview of various types of hydrogen production is given. The fundamentals of proton-conducting ceramic membranes and their applications in PCMRs for SMR and reversible PCEC (RePCEC), respectively, are given. In particular, RePCECs are of particular interest when renewable power generation exceeds demand because the excess electrical energy is converted to chemical energy in the electrolysis cell mode, therefore representing an appealing solution for energy conversion and grid-scale storage.

Keywords: proton-conducting ceramic membranes; hydrogen; decarbonized heat; joule heating; membrane reactors; electrolysis



Citation: Buonomenna, M.G. Proton-Conducting Ceramic Membranes for the Production of Hydrogen via Decarbonized Heat: Overview and Prospects. *Hydrogen* **2023**, *4*, 807–830. <https://doi.org/10.3390/hydrogen4040050>

Academic Editor: Wei Wang

Received: 19 August 2023

Revised: 17 September 2023

Accepted: 5 October 2023

Published: 13 October 2023



Copyright: © 2023 by the author. Licensee MDPI, Basel, Switzerland. This article is an open access article distributed under the terms and conditions of the Creative Commons Attribution (CC BY) license (<https://creativecommons.org/licenses/by/4.0/>).

1. Introduction

The world faces fundamental choices that will determine whether in the framework of global warming the 1.5 °C path, as defined at COP26, will remain within reach. Electrification and efficiency are key resulting in a cut of nearly 37 gigatonnes in annual CO₂ emissions by 2050 [1]. These reductions can be achieved through (1) increases in production and uses of renewables-based electricity; (2) improvements in energy efficiency [2]; (3) electrification of end-use sectors such as electric vehicles and heat pumps; (4) clean hydrogen and its derivatives [3,4]; (5) bioenergy coupled with carbon capture and storage [5]; and (6) the use of carbon capture and storage (Figure 1).

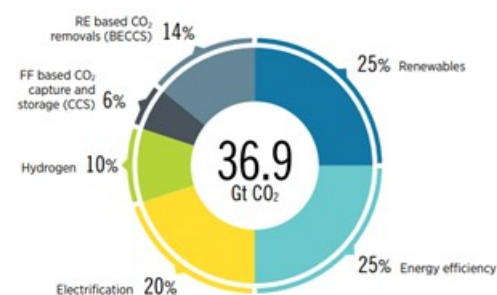


Figure 1. Reducing emissions by 2050 through six technological avenues [1].

In this context, the decarbonization of heat is a cross-cutting opportunity. Many recent studies have emphasized its crucial role [6–8]. Indeed, a large portion of industrial

sector emissions, estimated at about 7.5 Gt of CO₂ [9], about 21% of global greenhouse gas (GHG) emissions [10], derive from the generation of over 100 EJ_{th} of thermal energy. The combustion of three fuels, i.e., coal, natural gas and oil, generates the vast majority of this heat and it's associated with CO₂ emissions.

Thiel and Stark [11] discussed four strategies for decarbonizing heat production, i.e., zero-carbon fuels, zero-carbon heat sources, the electrification of heat and better heat management, as schematized in Figure 2.

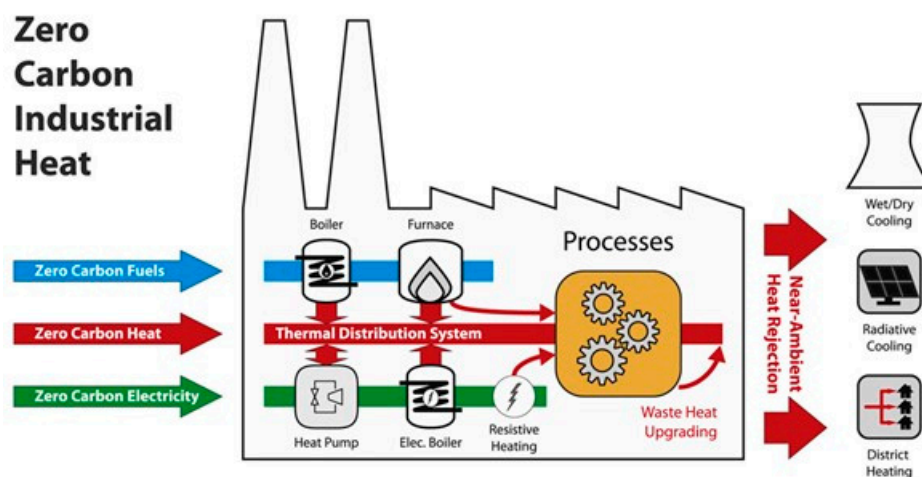


Figure 2. Schematic representation of technologies to enable zero-carbon industrial heat through the utilization of zero-carbon fuels, zero-carbon heat, electrification of heat, and better heat management technologies. Reproduced from [11] with permission of Elsevier.

Among these four pathways, there is electrification of heat, i.e., the generation of thermal energy from electricity. It must be emphasized that the greenhouse gas benefits of the electrification of heat are strictly related to grid decarbonization; in other words, electrified heat is decarbonized heat only when electricity is generated without carbon emissions. As the grid moves toward 100% low-carbon electricity, the GHG benefits of electrification will increase, but until then, it is important to recognize the proportion of low-carbon energy in the grid to understand the magnitude of electrification benefits in the near future [1]. Even though a rapid increase in power generation from solar and wind was observed covering in summer up to 30–40% of the total energy demand at the expense of traditional energy sources from fossil fuels [12], the intermittent nature of these renewable energies has hastened the need for low-cost storage over a wide range of time scales, from seconds to days and even seasonal storage. Energy storage systems as well as decarbonizing industrial processes are two current grand challenges to be faced [7]. In addition to direct electrical energy storage such as pumped hydroelectricity, batteries, flow batteries [13], compressed air and emerging options with direct ties to the grid [14], there is the indirect approach of converting variable energy like wind and solar to energy carriers (chemical energy) such as hydrogen (H₂), ammonia, and ethanol, storing and transporting those energy carriers, and then using them in industry. In this context, the use of electrolysis fed by renewable energy to produce low-carbon energy carriers such as H₂, and the use of those chemicals as fuels, reductants, feedstock, and for upgrading petroleum products in refining, represents a low-carbon pathway to net-zero GHG emissions for a number of industrial processes [8].

In this paper, an overview of recent advances in the production of hydrogen within the framework of decarbonizing heat by means of proton-conducting ceramic membranes is given. In particular, after a section on hydrogen production, some general considerations on proton-conducting ceramic membranes as well as types of proton-conducting ceramic membranes and their applications in membrane reactors (MRs) and reversible protonic ceramic electrochemical cells (PCECs) are reported.

2. Hydrogen Production

The energy industry uses color codes to differentiate hydrogen on the basis of the type production.

Across a spectrum of carbon intensity (Figure 3), there is black and brown hydrogen using black coal or lignite (brown coal) in the hydrogen-making process and green hydrogen, which is made by using clean electricity from surplus renewable energy sources, such as solar or wind power, in water electrolysis [15–17] (discussed below). The black and brown hydrogen, which are the opposite of green hydrogen, are the most environmentally damaging.

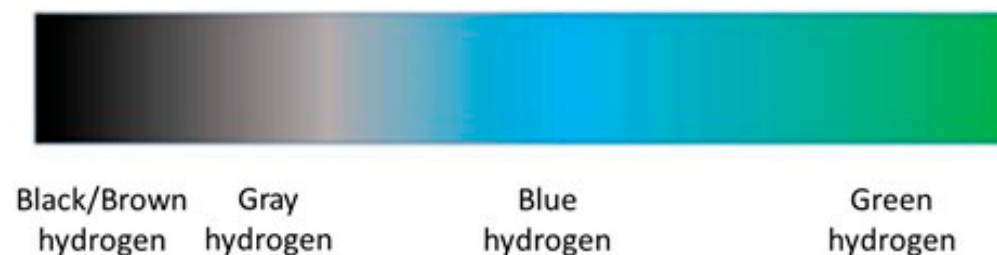


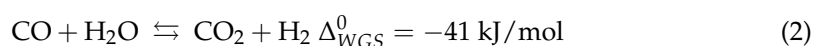
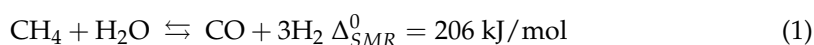
Figure 3. Spectrum of molecular hydrogen on the basis of its production.

Currently, gray hydrogen is the most common form of hydrogen production: it is obtained from natural gas, or methane, using steam methane reforming (SMR) (discussed below), but without capturing the greenhouse gases made in the process. Blue hydrogen is essentially the same as gray hydrogen, but includes the use of carbon capture and storage (CCS) to trap and store the CO₂ produced in the process. Moreover, there are relatively new hydrogen codes such as yellow hydrogen, turquoise hydrogen and pink hydrogen. Yellow hydrogen indicates hydrogen made through electrolysis using solar power. Turquoise hydrogen is made using a methane pyrolysis to produce hydrogen and solid carbon. In the future, such type of hydrogen may be valued as a low-emission hydrogen, if the thermal process is powered with renewable energy and the carbon being permanently stored. Pink hydrogen is generated through electrolysis powered by nuclear energy. In addition, the very high temperatures from nuclear reactors could be used in other hydrogen productions by producing steam for more efficient electrolysis or fossil-gas-based steam methane reforming [18].

The current cost for green H₂ is five to seven times that of gray H₂ and three times that of blue H₂, but such cost difference is expected to narrow with increased development and scale [19]. The CO₂ reduction between an electrolytic H₂ via grid-supplied electricity and gray H₂ is around 20–30%. For industry, H₂ via electrolysis using low-carbon sources could drive a much larger drop in CO₂ emissions [8].

2.1. SMR

Today, industrial-scale H₂ is produced via SMR, which supplies a range of chemical industries including synthesis of ammonia via the Haber-Bosch process, fuels and methanol. In SMR, natural gas (methane) reacts with steam according to the following equations:



The synthesis gas known as syngas (CO + H₂) composition is governed by the methane reforming reaction (1) and the water–gas shift (2). Syngas conversion processes occur at high pressure and therefore, process economy favors operating the SMR at high pressure to decrease compression cost in the plant design. However, looking at the stoichiometry of the reaction (1), SMR is adversely impacted by high pressure due to Le Chatelier principle,

shifting the equilibrium to left. Consequently, high temperatures are required to drive the reaction. Typical conditions are 30 bar and 900 °C [20]. A large-scale industrial reformer can contain up to several hundred tubular reactors in a large furnace, favored for uniform distribution of heat, which is produced by combustion of fossil fuels [20]. For most large-scale industrial reformers, radiation is the primary heat-transfer mechanism. Therefore, the combustion process must occur several hundred degrees above the reaction temperature to supply the necessary heat flux for the catalyst [20–22].

A typical large-scale industrial syngas plant for pure H₂ production has several reaction units, being steam-reforming equilibrium-limited and even, in the case of complete fuel conversion, a hydrogen-rich gas mixture containing carbon oxides and other by-products is produced. Typically, a high-temperature reformer, high- and low-temperature shift reactors with subsequent separation and compression downstream via pressure swing adsorption to separate H₂ from CO₂ feature an industrial steam reforming plant (Figure 4).

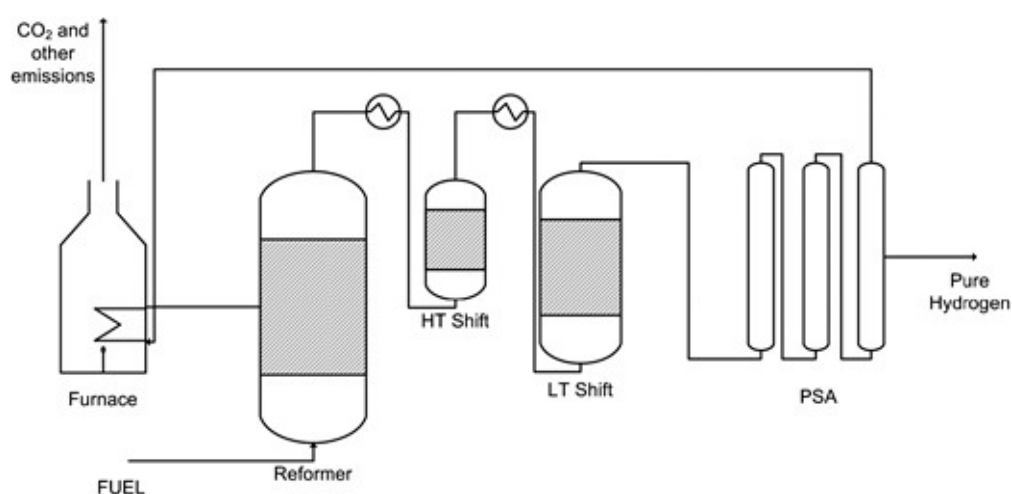


Figure 4. Conventional steam reforming reaction scheme. HT shift and LT shift are high- and low-temperature shift reactors, respectively. Reproduced from [23] with permission of Elsevier.

A typical fired SMR process based on natural gas emits 7–11 kg CO₂/kg H₂ [24]. The global production of syngas accounts for nearly 3% of global CO₂ emissions [25,26]. The heat source can be a variety of hydrocarbons with a high to low carbon content, i.e., from coal or coke to natural gas to renewables. In the context of decarbonized heat, i.e., to replace the fossil fuel combustion, excess electric power electricity from renewables can be transformed into heat via microwaves, induction, joule heating, or plasma (Figure 5).

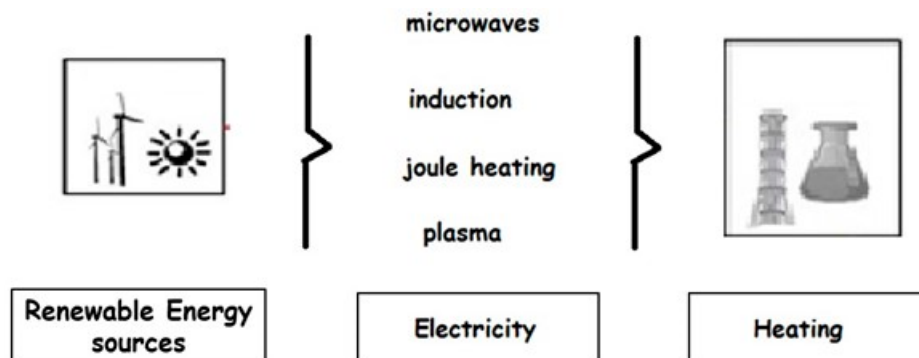


Figure 5. Converting renewable energies power into heat can decarbonize industrial processes for the production of chemicals.

Several studies have investigated relevant endothermic processes proposing electrified heat as listed in Table 1.

Table 1. Selected studies on strategies of electrification of endothermic processes to produce H₂.

Entry #	Process	Electrified Heat Transformation Route	Refs.
1	SMR	Induction	[27–29]
2	SMR	Joule heating	[24,26,30–33]
3	SMR	Plasma	[34]
4	Dry reforming of methane	Plasma	[34,35]
5	Biogas reforming	Induction	[36]
6	Dry reforming of methane	Microwave	[37]
7	Catalytic decomposition of methane	Plasma	[34]
8	Methane conversion to higher hydrocarbons	Microwave	[38]
9	Methane conversion to higher hydrocarbons	Plasma	[39]
10	CO ₂ reforming	Microwave	[38]
11	CO ₂ reforming	Joule heating	[40,41]
12	Decomposition of ammonia	Joule heating	[42]
13	Decomposition of ammonia	Plasma	[43,44]
14	Decomposition of ammonia	Microwave	[45,46]

In particular, joule heating instead of heating from fossil fuel combustion has been proposed for highly endothermic chemical synthesis such as SMR (Table 1) as discussed below. Notably, electrified heat is only decarbonized heat when the electricity is generated without carbon emissions [11]. Therefore, hydrogen synthesis from methane should include carbon capture converting emitted carbon dioxide into valuable commodity chemicals (Figure 6).

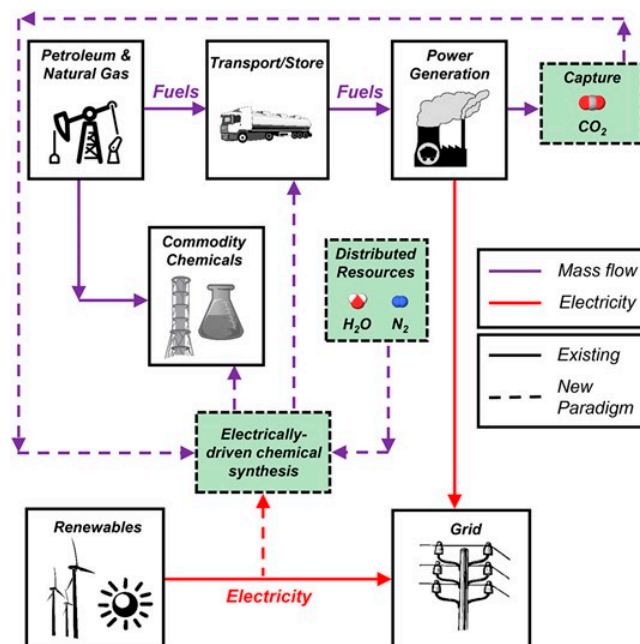


Figure 6. Current and envisioned coupling of the chemical and energy industry. Reproduced from [6] with permission of Elsevier.

2.2. Water Electrolysis

Another relevant strategy to produce hydrogen via decarbonized heat is by water electrolysis fed by renewable electric energy, which in other words is transforming renewable electric energy into chemical energy by producing feedstocks such as H₂ (Figure 6).

By sourcing hydrogen exclusively by electrolysis instead of by SMR would avoid the generation of CO₂ altogether.

Hydrogen produced by electrolysis can be used for several purposes ranging from low-carbon heating to the synthesis of chemicals, representing a relatively new opportunity to reduce our dependence on carbon-based sources of heat and feedstock. Water electrolysis is a well-established mature technology used in special applications [47]. The overall electrolysis reaction is the electrochemical splitting of water molecules, owing to an electric current between cathode and anode, separated by electrolyte.



Electrolytic hydrogen production technology can be classified on the basis of the employed ionic conductor, i.e., alkaline electrolysis cells (AECs), polymer electrolyte membrane electrolysis cells (PEMECs), protonic ceramic electrolysis cells (PCECs), and solid oxide electrolysis cells (SOECs). An overview of the four types of electrolytic hydrogen production technology is given in Table 2. In particular, AECs conventionally operate at lower temperatures in the range of 25–100 °C and utilize a concentrated alkaline solution as a medium for the conduction of hydroxide ions (OH[−]), which is fed to the cathode and anode for the corresponding hydrogen evolution reaction (HER) (Equation (4)) and oxygen evolution reaction (OER) (Equation (5))



To avoid the mixing of the produced H₂ and O₂ (Equations (4) and (5)), a separator is typically placed between the electrodes, generally a polyphenylene sulfide (PPS)-based diaphragms [48] for which the main drawbacks are a limited current density (normally below 400 mA·cm^{−2}) and an insufficient energy efficiency [49].

In the case of PEMECs, the conducted ion is proton (H⁺) transported through a polymer electrolyte membrane, while the deposited electrocatalysts promote the HER and OER on both sides as reported in Equations (6) and (7):



Additionally, PCECs use H⁺ as the conducted ion in electrolyte materials (with identical HER and OER expressions to those shown in Equations (6) and (7)), whilst the operating temperatures are in the range of 550–700 °C, requiring very different cell structures and material selections. The electrolyte materials mainly comprise proton conducting ceramic membranes as discussed below in this review, whereas cermet materials incorporating metals are utilized as electrocatalysts for remarkable catalytic activity.

SOECs have similar structures and materials to PCECs with a further increase in the working temperature to >700 °C, whereas the ion conduction in the electrolyte is dominated by the migration of oxygen ions (O^{2−}), which requires a water supply to the hydrogen electrode (cathode) and involves distinct HER and OER expressions, as reported in Equations (8) and (9):



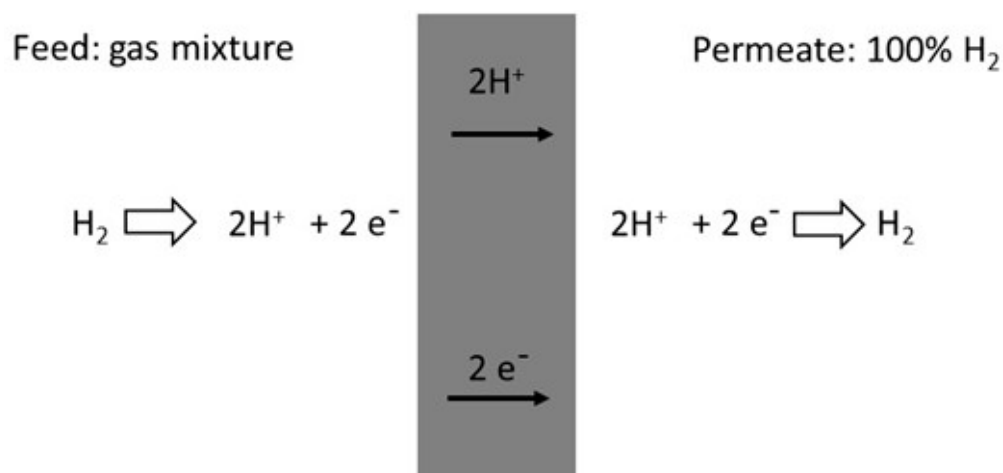
Table 2. Specification of AECs, PEMECs, PCECs and SOECs (adapted from [49] with permission of American Chemical Society).

	AECs	PEMECs	PCECs	SOECs
HER	$2\text{H}_2\text{O} + 2\text{e}^- \rightarrow \text{H}_2 + 2\text{OH}^-$	$2\text{H}^+ + 2\text{e}^- \rightarrow \text{H}_2$	$2\text{H}^+ + 2\text{e}^- \rightarrow \text{H}_2$	$\text{H}_2\text{O} + 2\text{e}^- \rightarrow \text{H}_2 + \text{O}^{2-}$
OER	$2\text{OH}^- \rightarrow 1/2 \text{O}_2 + \text{H}_2\text{O} + 2\text{e}^-$	$\text{H}_2\text{O} \rightarrow 1/2 \text{O}_2 + 2\text{H}^+ + 2\text{e}^-$	$\text{H}_2\text{O} \rightarrow 1/2 \text{O}_2 + 2\text{H}^+ + 2\text{e}^-$	$\text{O}^{2-} \rightarrow 1/2 \text{O}_2 + 2\text{e}^-$
Charge carrier	OH^-	H^+	H^+	O^{2-}
Electrolyte	NaOH/KOH solution	Polymers	Ceramics	Ceramics
Electrocatalyst	Ni	Pt/C IrO ₂	Ceramics and cermets	Ceramics and cermets
Temperature (°C)	25–100 (low range) 100–250 (high range)	25–100 (low range) 100–250 (high range)	550–700	>700

3. Proton Conducting Ceramic Membranes: General Considerations

Membrane technologies have all the features of process intensification strategy, i.e., low energy consumption, easy scalability, modularity [50]. In particular, H₂ separation using membranes can operate continuously using potentially less than half the energy required for the PSA process at the downstream of SMR (Figure 4) [51]. Among the four kinds of hydrogen separation membranes (polymeric, metallic, carbon, and ceramic [52]), only polymeric membranes have been in commercial use to any considerable extent at the current state of technology. Among the three inorganic categories, i.e., metallic, carbon and ceramic, proton–electron conducting ceramic membranes are the most promising due to their two main advantages, i.e., high selectivity and low cost [53]. Indeed, proton–electron–conducting ceramic membranes are permeable only to hydrogen ions, i.e., protons allowing the extraction of hydrogen from gas mixtures with a theoretical selectivity of 100%.

Overall, the process of H₂ transport through a proton–electron–conducting ceramic membrane mainly involves two steps, as schematized in Figure 7: (i) H₂ is first adsorbed onto the surface of the membrane, then dissociates into protons and electrons (surface process); (ii) protons and electrons diffuse together to the other side of the membrane surface where they reassociate to form molecular H₂ again (bulk diffusion) [54].

**Figure 7.** Schematic of transport through a protonic conducting ceramic membrane.

The permeation of hydrogen through the membrane is primarily controlled by the surface process and bulk diffusion.

Regarding bulk diffusion, the transport of protons through the membrane is the rate-determining step if the electron conductivity is much higher than the proton conductivity. Taking into account the chemical/electrochemical potentials and conductivities of both

protons and electrons within the membrane, the H₂ flux (J_{H2}) can be described by the Wagner equation as follows [55]:

$$J_{H_2} = \frac{RT}{4F^2l} \frac{\sigma_{H^+}\sigma_{el}}{\sigma_{H^+} + \sigma_{el}} \ln\left(\frac{P'_{H_2}}{P''_{H_2}}\right) \quad (10)$$

where R is the universal gas constant, T is the temperature, F is the Faraday constant, l is the thickness of the ceramic membrane, σ_{H^+} is the proton conductivity within the membrane, σ_{el} is the sum of the electron and hole conductivities, P'_{H_2} is the H₂ pressure at upstream membrane and P''_{H_2} is the H₂ pressure at downstream membrane (Figure 7). Proton and electron conductivities as well as the temperature and pressure at the membrane upstream and downstream as well as membrane thickness control the H₂ flux.

Two opposite cases can occur.

The first is when the proton conductivity σ_{H^+} within the membrane is much smaller than the electron conductivity σ_{el} ; that is $\sigma_{H^+} \ll \sigma_{el}$, Equation (10) can be rewritten as:

$$J_{H_2} = \frac{RT}{4F^2l} \sigma_{H^+} \ln\left(\frac{P'_{H_2}}{P''_{H_2}}\right) \quad (11)$$

In this case, the development of highly conductive proton-conducting ceramic membranes is very important for achieving high H₂ flux as discussed below.

The second case is if the proton conductivity within the membrane is much larger than the electron conductivity, i.e., $\sigma_{H^+} \gg \sigma_{el}$. So, Equation (10) can be rewritten as:

$$J_{H_2} = \frac{RT}{4F^2l} \sigma_{el} \ln\left(\frac{P'_{H_2}}{P''_{H_2}}\right) \quad (12)$$

In this case, ceramic membranes with high electron conductivity become crucial in achieving high H₂ flux during the separation process.

Normally, it is difficult to obtain both high proton and high electron conductivities. This depends on the membrane materials.

Different types of ceramic H₂ separation membranes are reported in the literature:

- (1) Cermet membranes, consisting of a combination of a ceramic phase and a metallic phase. The metal is used as the electron-conducting phase and the ceramic oxide serves as the proton-conducting phase. Combining these two phases together may lead to high h₂ permeation because both σ_{h^+} and σ_{el} are high;
- (2) Single-phase ceramic oxides membranes, which simultaneously transport protons and electrons.
- (3) Cer-cer membranes, i.e., dual-phase ceramic oxides membranes, which combine a protonic conducting perovskite phase and electronic (non-perovskite) phase.

Single-phase ceramic membranes in turn may be classified into two subcategories: perovskite-type and non-perovskite-type membranes.

A scheme of the various types of proton conducting ceramic membranes is shown in Figure 8. In Table 3 a comparison of thickness normalized H₂ permeation flux of ceramic membranes from the literature is given.

3.1. Perovskite-Type Ceramic Membranes

The term perovskite originally refers to a mineral calcium titanium oxide, CaTiO₃. Today perovskite-type metal oxides is the name given to a group of materials with general formula ABO_3 (Figure 9) having the same structure as the mineral calcium titanate (CaTiO₃) [56]. In this general formula, $A = Ca, Ba, Sr$; $B = Ce, Zr$. The distance between the oxygen ions, which plays an important role in proton conductivity, can be changed by doping a trivalent M element into the structure leading to a significant improvement [57]. The formula of these high-temperature, proton-conducting perovskite oxides can be written as $AB_{1-x}M_xO_{3-\delta}$. Doping a trivalent M cation into the B site can increase the vibration

distance between the oxygen ions and also create more oxygen vacancies, leading to higher proton conductivity [58–60]. The most studied high temperature perovskite-type oxides are SrCeO_3 and BaCeO_3 , which have high protonic conductivity but poor electronic conductivity. Electron conductivity has been improved by doping the *B* site in SrCeO_3 and BaCeO_3 with a multivalent cation [61–63]. Moreover, BaCeO_3 and SrCeO_3 are chemically unstable, easily reacting with CO_2 and H_2O [64–66]. In particular, formation of undesired phases such as carbonates would be formed because of the reaction between alkali earth ions, i.e., Ba^{2+} and Sr^{2+} and CO_2 at elevated temperature. This is the weak point of ceramic-based membranes, while the drawback of Pd-based membranes (not discussed in this paper) is hydrogen-induced embrittlement and sulfur poisoning.

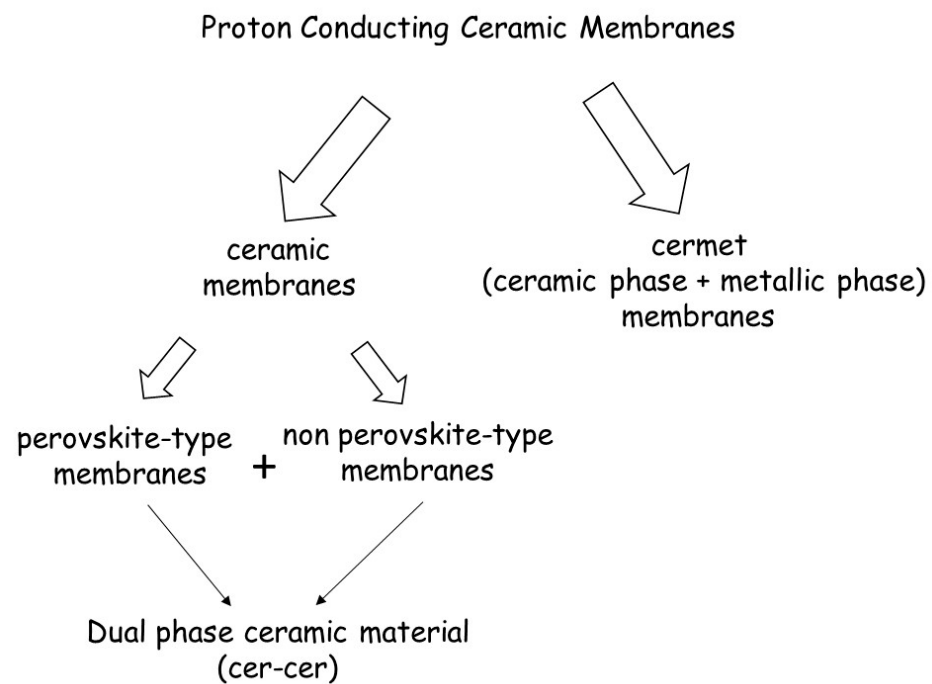


Figure 8. Schematic of the various types of proton-conducting ceramic membranes.

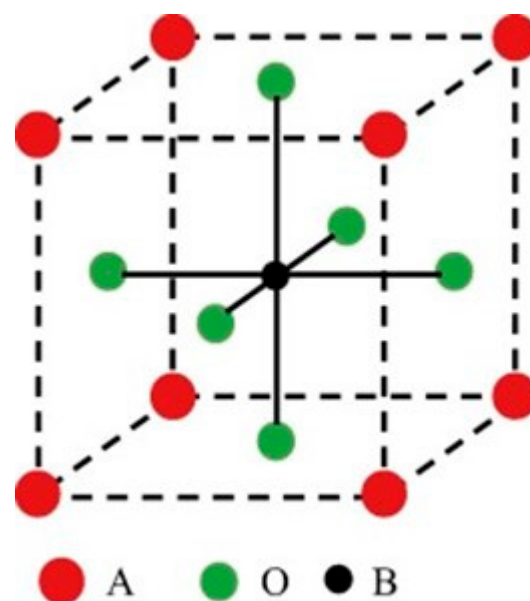


Figure 9. ABO_3 perovskite structure. Reproduced from [67] with permission of Elsevier.

In contrast, zirconate-based proton-conducting perovskite oxides are stable, but their conductivity is limited by highly resistive grain boundaries [68,69]. Indeed, the total conductivity of Y-doped BaZrO₃, the most promising zirconate in H₂O and CO₂-containing atmospheres, decreases sharply, owing to the blocking effect of grain boundaries combined with the small grain sizes in these materials [69]. In order to develop advanced membrane materials, solid solutions of cerate and doped zirconate (Y-doped BaZrO₃-BaCeO₃) have been investigated. Yttrium-doped barium zirconate/cerate materials (BaCe_xZr_{1-x-y}Y_yO_{3-d}, BCZY) represent the best compromise between the high proton conductivity of cerate-based and high stability of zirconate-based proton conducting perovskite oxides. They are stable over a wide range of temperatures (300–800 °C) and chemical environments and are among the most studied materials for hydrogen separation membranes in membrane reactors (MRs) [70–74] and reversible protonic ceramic electrochemical cells (PCECs) [75,76] as discussed below.

3.2. Non-Perovskite-Type Ceramic Membranes

The non-perovskite type membranes for hydrogen separation are mainly doped rare earth metal oxides and fluorite-structured metal oxide. Alkali earth ion-free oxides such as LaNbO₄, Ln₆WO₁₂, Y₂O₃, CeO₂ were developed in order to overcome the drawback of other phase formation such as carbonates under a CO₂ rich atmosphere. Ln₆WO₁₂ presents relatively high mixed protonic and electronic conductivities and reasonable stability under CO₂ and H₂O [77]. Moreover, among the Ln₆WO₁₂-based membrane materials, Mo-doped, Nd_{5.5}WO_{11.25-d}, and Re-doped materials showed almost the highest ambipolar conductivity and hydrogen permeation flux.

3.3. Cer-Cer Dual-Phase Ceramic Membranes

As reported by Elangovan et al. [78], H₂ permeating material with high performance can be obtained by combining (i) a protonic conducting perovskite phase BaCe_{1-x}M_xO_{3-d} and (ii) an electronic conducting fluorite phase Ce_{1-y}M_yO_{2-d} (M is the metal dopant). Such combination is named as *cer-cer* composite. It has certain degree of percolation, which provides efficient pathways for proton and electronic transport through the membrane. In such systems (Table 3), the addition of the doped ceria phase enhances the stability of BaCeO₃ phase, which otherwise, in the presence of CO₂ and H₂O, would decompose to BaCO₃, Ba(OH)₂ and CeO₂.

3.4. Cermet Membranes

In cermet membranes, a ceramic phase is combined with a metallic phase in order to enhance H₂ permeation because the ceramic phase is a proton conductor and the metallic phase is a highly electron conductor. Depending on the degree of hydrogen conductivity in the metal phase, mainly three different combinations can be realized [23]: (i) a metal with low hydrogen conductivity in combination with a highly proton-conductive oxide; (ii) a metal or an alloy with high hydrogen permeability such as Pd, Pd/Ag, Pd/Cu, Pd/Cu, combined with a ceramic of low hydrogen permeability; (iii) a combination where both the metallic and ceramic phases conduct hydrogen.

Table 3. Thickness-normalized values of H₂ permeation rates (J_{H2}) through ceramic membranes (adapted from [53] under CC-BY 4.0).

Material	Gas Atmosphere Feed-Sweep	T (°C)	J _{H2} , Norm (mL·min ⁻¹ ·cm ⁻¹)	Ref.
<i>Perovskite ceramic membranes</i>				
BaCe _{0.80} Y _{0.10} Ru _{0.10} O _{3-δ}	wet H ₂ in Ar–Ar	800	4.3 × 10 ⁻³	[79]
BaCe _{0.95} Nd _{0.05} O _{3-δ}	wet 80% H ₂ in He–dry Ar + Ne	900	1.3 × 10 ⁻³	[80]
BaZr _{0.80} Y _{0.15} Mn _{0.05} O _{3-δ}	wet 50% H ₂ in He–wet Ar	900	1.4 × 10 ⁻³	[81]
SrCe _{0.95} Tm _{0.05} O _{3-δ}	10% H ₂ in He–air	700–900	1.2 × 10 ⁻³ /1.9 × 10 ⁻³	[82]
SrCe _{0.95} Tm _{0.05} O _{3-δ}	10% H ₂ in He–air	700–900	2.6 × 10 ⁻³ /6.4 × 10 ⁻³	[83]

Table 3. Cont.

Material	Gas Atmosphere Feed-Sweep	T (°C)	Norm J_{H_2} (mL·min ⁻¹ ·cm ⁻¹)	Ref.
SrCe _{0.95} Tm _{0.05} O _{3-δ}	10% H ₂ dry in He–20% O ₂ in Ar	750/900	$4.3 \times 10^{-3}/6.8 \times 10^{-3}$	[84]
SrCe _{0.95} Tb _{0.05} O _{3-δ}	20% H ₂ in He–CO in Ar	750/900	$4.0 \times 10^{-4}/1.6 \times 10^{-3}$	[85]
SrCe _{0.95} Y _{0.05} O _{3-δ}	80% H ₂ in He–Ar	900	3.2×10^{-4}	[86]
SrCe _{0.95} Y _{0.05} O _{3-δ}	10% H ₂ in He–air	677	2.7×10^{-3}	[87]
SrCe _{0.95} Eu _{0.05} O _{3-δ}	100% H ₂ –He	700–850	$2.3 \times 10^{-4}/7.4 \times 10^{-4}$	[88]
SrCe _{0.95} Sm _{0.05} O _{3-δ}	100% H ₂ –He	850	5.4×10^{-4}	[88]
SrCe _{0.75} Zr _{0.20} Tm _{0.05} O _{3-δ}	H ₂ in He–wet Ar	750/900	5.0×10^{-3}	[89]
SrCe _{0.75} Zr _{0.20} Tm _{0.05} O _{3-δ}	10% H ₂ dry in He–20% O ₂ in Ar	900	$8.0 \times 10^{-4}/2.4 \times 10^{-3}$	[84]
SrCe _{0.70} Zr _{0.25} Ln _{0.05} O _{3-δ} (Ln = Tm, Yb)	wet 20% H ₂ –wet sweep (not specified)	900	2.3×10^{-4}	[90]
SrCe _{0.65} Zr _{0.20} Eu _{0.15} O _{3-δ}	100% H ₂ –He	900	8.5×10^{-4}	[91]
SrZr _{0.95} Y _{0.05} O _{3-δ}	20% H ₂ –air in He	700	$<2.3 \times 10^{-5}$	[87]
<i>Non-perovskite ceramic membranes</i>				
La _{5.5} WO _{11.25-δ}	wet 50% H ₂ in He–wet Ar	750/900	$1.5 \times 10^{-3}/4.7 \times 10^{-3}$	[92]
La _{5.5} W _{0.8} Mo _{0.2} O _{11.25-δ}	wet 50% H ₂ in He–wet Ar	700	2.7×10^{-3}	[92]
La _{5.5} W _{0.8} Re _{0.2} O _{11.25-δ}	wet 50% H ₂ in He–wet Ar	700	5.9×10^{-3}	[92]
Nd _{5.5} WO _{11.25-δ}	wet 20% H ₂ in He–wet Ar	1000	1.2×10^{-3}	[93]
(Nd _{5/6} La _{1/6}) _{5.5} WO _{12-δ}	wet 50% H ₂ in He–wet Ar	900	1.2×10^{-3}	[94]
(La _{5/6} Nd _{1/6}) _{5.5} WO _{12-δ}	wet 50% H ₂ in He–wet Ar	900	1.4×10^{-3}	[95]
Nd _{5.5} W _{0.5} Mo _{0.5} O _{11.25-δ}	wet 50% H ₂ in He–wet Ar	900	7.5×10^{-3}	[96]
Nd _{5.5} W _{0.5} Re _{0.5} O _{11.25-δ}	wet 50% H ₂ in He–wet Ar	900	4.1×10^{-3}	[97]
<i>Cer-Cer dual phase membranes</i>				
La _{5.5} WO _{11.25-δ} :La _{0.87} Sr _{0.13} CrO _{3-δ} (50:50 vol.%)	wet 50% H ₂ in He–wet Ar	700	5.5×10^{-3}	[98]
BaCe _{0.80} Eu _{0.20} O _{3-δ} :Ce _{0.80} Eu _{0.20} O _{2-δ} (50:50 vol.%)	H ₂ , CH ₄ , H ₂ O, CO, CO ₂ –He	900	$<7.0 \times 10^{-2}$	[78]
BaCe _{0.80} Y _{0.20} O _{3-δ} :Ce _{0.80} Y _{0.20} O _{2-δ} (50:50 wt.%)	wet 50% H ₂ in He–wet Ar	900	1.1×10^{-2}	[99]
BaCe _{0.65} Zr _{0.20} Y _{0.15} O _{3-δ} :Ce _{0.85} Gd _{0.15} O _{2-δ} (50:50 vol.%)	wet 50% H ₂ in He–wet Ar	755	1.76×10^{-2}	[100]
BaCe _{0.20} Zr _{0.70} Y _{0.10} O _{3-δ} :Sr _{0.95} Ti _{0.90} Ni _{0.10} O _{3-δ} (50:50 vol.%)	9% H ₂ in He–dry Ar	800	1.1×10^{-3}	[101]
SrZrO ₃ :SrFeO ₃ (80:20 vol.%)	H ₂ in He–wet Ar	900	4.8×10^{-3}	[102]
<i>Cermet membranes</i>				
BaCe _{0.95} Tb _{0.05} O _{3-δ} :Ni (50:50 wt.%)	50% H ₂ in N ₂ –He	850	8.3×10^{-3}	[103]
BaCe _{0.90} Y _{0.10} O _{3-δ} :Ni (60:40 vol.%)	4% H ₂ in He–100 ppm H ₂ in N ₂	800	1.7×10^{-2}	[104]
BaCe _{0.80} Y _{0.20} O _{3-δ} :Ni (60:40 vol.%)	3.8% H ₂ in N ₂ –100 ppm H ₂ in N ₂	900	2.0×10^{-3}	[105]
BaCe _{0.85} Zr _{0.10} Tb _{0.05} O _{3-δ} :Ni (50:50 wt.%)	50% H ₂ in 50% He–Ar	800	8.5×10^{-3}	[106]
BaCe _{0.70} Zr _{0.10} Y _{0.20} O _{3-δ} :Ni (60:40 vol.%)	4% H ₂ in He–100 ppm H ₂ in N ₂	900	5.6×10^{-3}	[107]
BaCe _{0.70} Zr _{0.10} Y _{0.10} Yb _{0.10} O _{3-δ} :Ni (60:40 vol.%)	20% H ₂ –wet, 60% CO ₂ , 20% He–N ₂	900	3.5×10^{-3}	[108]
Ce _{0.50} La _{0.4875} Ca _{0.0125} O _{2-δ} :Ni (60:40 vol.%)	wet 20% H ₂ , 77% N ₂ –Ar	900	1.5×10^{-3}	[109]
YSZ:Pd (40:60 vol.%)	90% H ₂ in He–N ₂	400/900	$4.7 \times 10^{-2}/9.4 \times 10^{-2}$	[110]

4. Applications of Proton-Conducting Ceramic Membranes to Produce Decarbonized H₂

Regarding hydrogen production, proton-conducting ceramic membranes are used in reversible fuel cells, i.e., Reversible Protonic Ceramic Electrochemical Cells (RePCECs), to produce both H₂ and electricity [111,112], in Proton Ceramic Membrane Reactors (PCMRs) for dehydrogenation of ethane to ethylene [71] and SMR [72–74]. Below some case studies are discussed.

4.1. PCMRs

Membrane reactors can be classified on the basis of the membrane role [113,114]. The membrane can have three different functions (Figure 10):

- (i). It can be used to extract a reaction product from the reaction zone in the so-called *extractor*.
- (ii). It can control the introduction of one of the reactants into the reaction zone in the so-called *distributor*.
- (iii). It can facilitate the contact between reactants and catalyst in the so-called *contactor*.

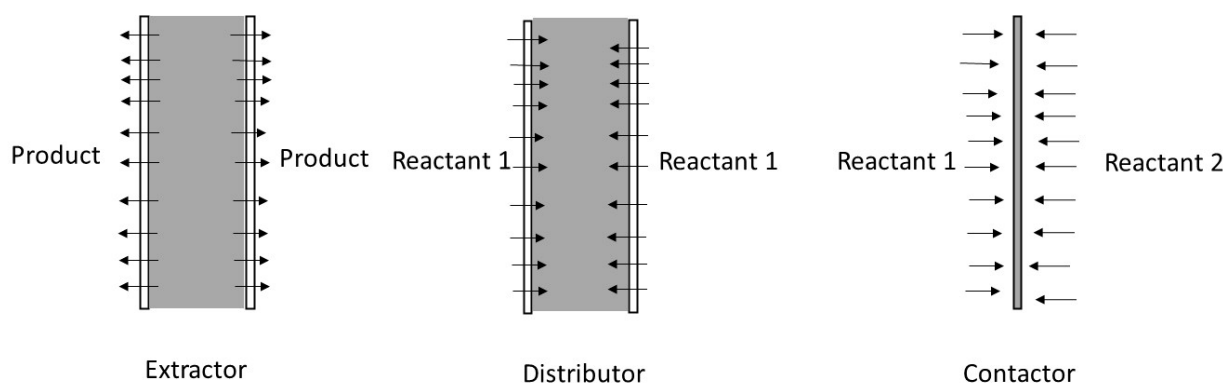


Figure 10. Different MRs in relation to membrane role.

All the case studies discussed below involve decarbonized hydrogen production concern extractor type MRs for SMR (Table 4, entries 1–3). Indeed, the reactions involved are equilibrium reactions and the membrane, which allow continuous removal of the H_2 product, i.e., its extraction; as a result increases the reaction conversion according to the Le Chatelier principle.

Table 4. Selected case studies of PCMRs.

Entry #	Reaction	Ceramic Membrane	Anodic Electrode	Cathodic Electrode	Temperature (°C)	Ref.
1	SMR	$BaZr_{0.7}Ce_{0.2}Y_{0.1}O_{2.9}$ $BaZr_{0.7}Ce_{0.2}Y_{0.1}O_{3-\delta}$	NiBZCY72 cermet	Cu	450–650	[74]
2	SMR	(BZCY72)/ $BaZr_{0.7}Ce_{0.1}Y_{0.2}O_{3-\delta}$ (BZCY71)/ $BaZr_{0.8}Ce_{0.1}Y_{0.1}O_{3-\delta}$ (BZCY81)	BCZY	Ni	800	[72]
3	SMR	$BaZr_{0.7}Ce_{0.2}Y_{0.1}O_{3-\delta}$ (BZCY72)/ $BaZr_{0.8}Ce_{0.1}Y_{0.1}O_{3-\delta}$ (BZCY81)	BCZY	Ni	750	[115]

In the specific case of SMR, with respect to a classical configuration consisting of a reaction unit in series with a separation unit, i.e., PSA (Figure 4), in an MR, the integration of a reaction to produce H_2 with its concomitant separation by the membrane reduces capital costs, improves yields and selectivities, and drastically reduces downstream separation costs [116]. In most studies, metallic membranes, predominantly based on Pd or Pd-Ag alloy are used [23,116]. The difference in hydrogen's chemical potential constitutes the driving force for hydrogen transport through the Pd membrane, from which it follows that even though complete methane conversion has been obtained, high pressures upstream are necessary and the pressure of the produced H_2 is low, and further compression requires multistage compressors, increasing energy consumption. In PCMR, protons are driven through the protonic ceramic membrane through the application of a voltage (or current) (Figure 11), which indirectly drives the flux of hydrogen gas (Figure 7) avoiding higher pressure. A gas mixture of methane saturated with steam is fed over the electrocatalyst (anode) where catalytic reactions (1)–(2) occur. With the use of an external power source, the produced hydrogen is extracted thanks its conversion at the anode in protons which are transported through the proton conducting ceramic membrane to the cathode according to the mechanism schematized above (Figure 7). At the cathode, protons recombine with electrons, forming molecular H_2 .

Kyriacou et al. [74] (Table 4, entry 1) used $BaZr_{0.7}Ce_{0.2}Y_{0.1}O_{2.9}$ perovskite as a proton-conducting membrane, a tubular NiBZCY72 cermet as anodic electrode, and a film of Cu as the cathode. The results showed that hydrogen migration was beneficial for methane conversion and hydrogen yield. Figure 12 shows the effect of proton removal from the anode on the increase in methane consumption. Initially, reacting methane correlates linearly with removed protons (under closed circuit operation). The experiments carried out to investigate the stability indicate suitable activity thanks to the outstanding $BaZr_xCe_{1-x}Y_{0.1}O_{3-\delta}$

perovskite membrane stability for $x > 0.3$ without the of formation barium carbonate as reported in the literature [117–119].

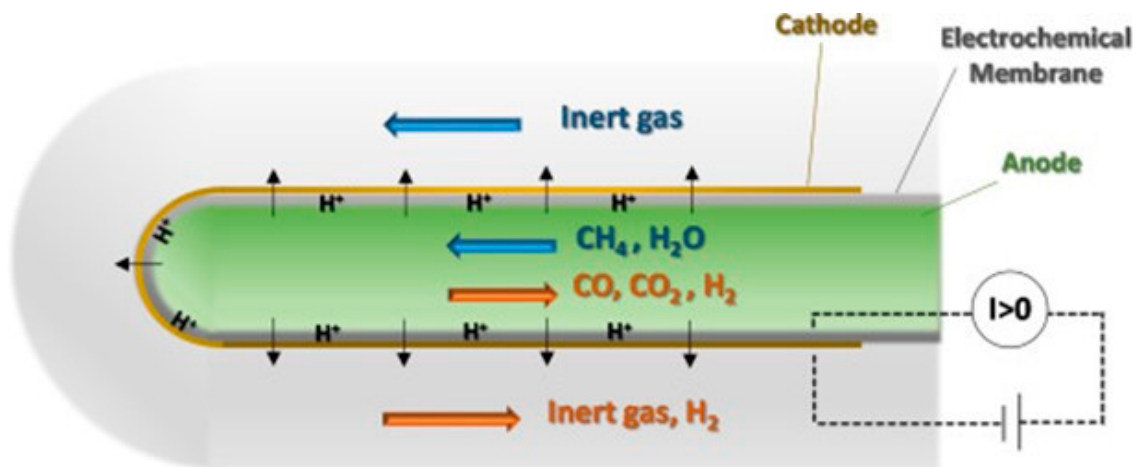


Figure 11. SMR concept in a PCMR. Reproduced from [74] with permission of Elsevier.

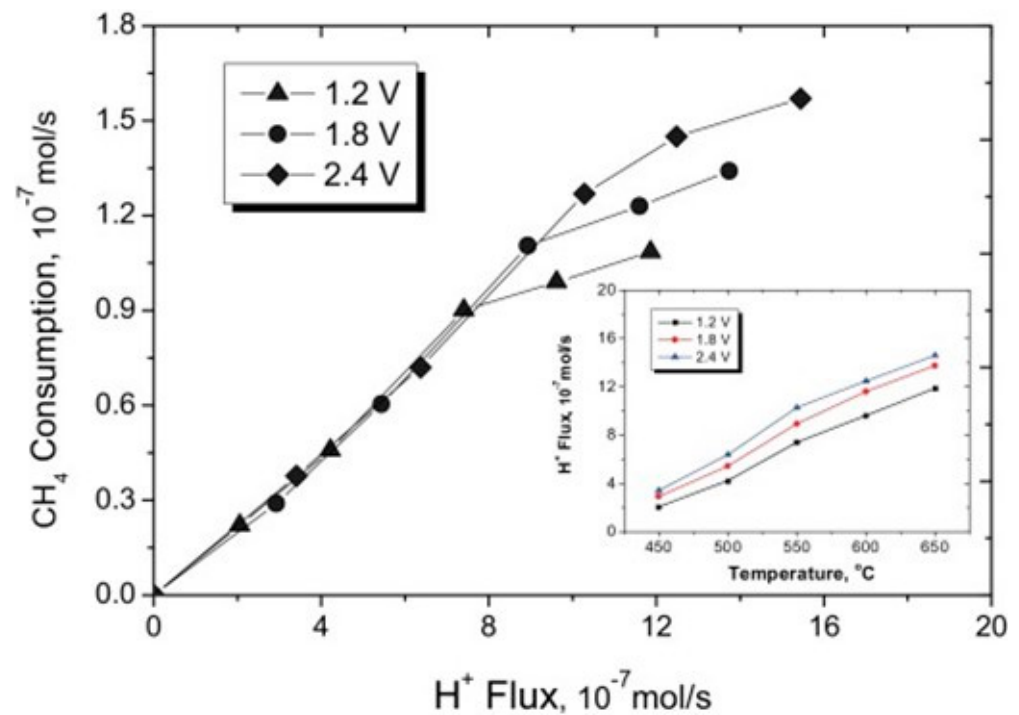


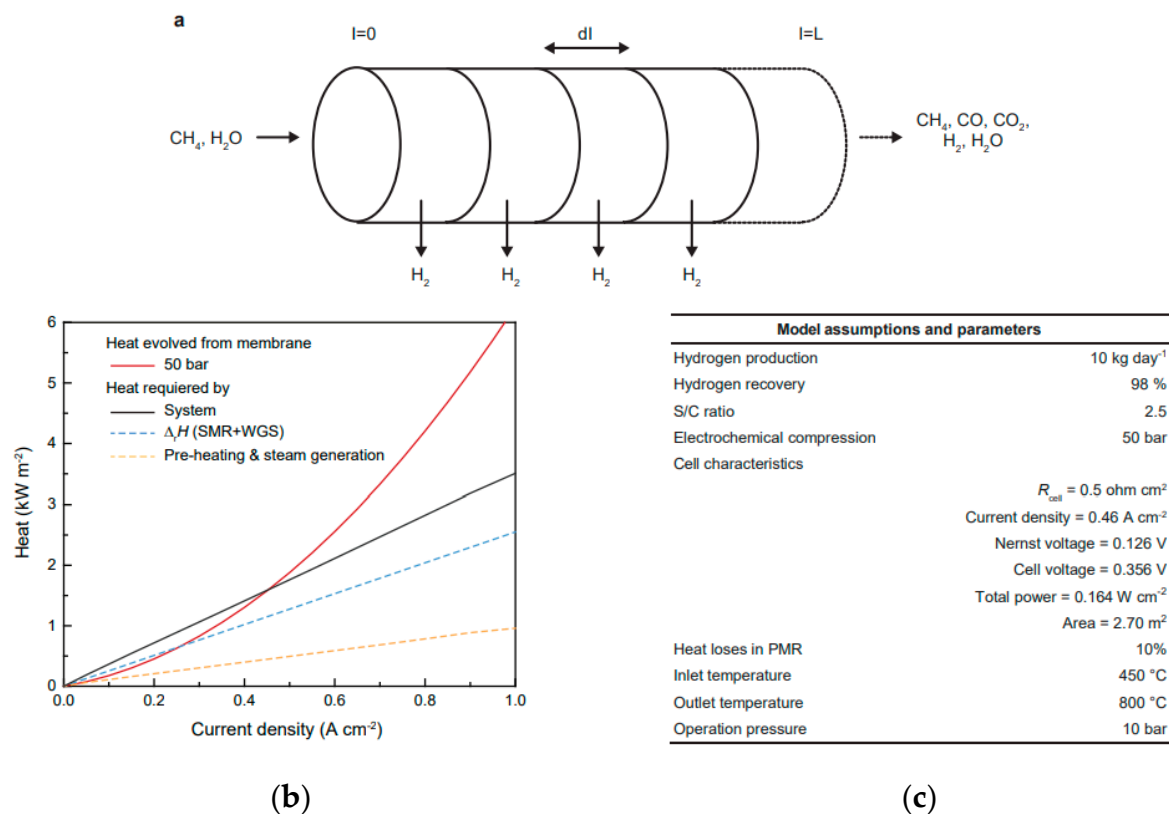
Figure 12. Dependence of the net closed-circuit methane consumption rate on proton flux through the BZCY72 membrane. Reproduced from [74] with permission of Elsevier.

Malerød-Fjeld et al. [72] proposed a PCMR operating at 800 °C and using a BaZrO₃-based proton conducting membrane (Table 4, entry 2). They simultaneously realized the extraction and shift of a thermodynamically limited reaction towards full conversion of methane and the production of high-purity H₂ as in MRs based on Pd membranes, but differently; on the latter, PCMR delivers heat to the strongly endothermic reaction (1) through the electrical operation of the membrane, which acts as separator and compressor, compressing hydrogen directly at the sweep side of the membrane. In Table 5 comparison of hydrogen production rate (J_{H_2}), methane conversion (X_{CH_4}), CO₂ selectivity (S_{CO_2}), and hydrogen recovery (HR) of PCMR with Pd-based membrane reformers is given.

Table 5. Comparison between Pd-based membrane reformers and PCMR investigated by Malerød-Fjeld et al. [72].

Reformer Type	J_{H_2} ($\text{mL min}^{-1} \text{cm}^{-2}$)	X_{CH_4} %	S_{CO_2} (%)	Temperature ($^{\circ}\text{C}$)	HR (%)	Ref.
Pd-based membrane	4–9	≤ 95	-	495–550	~ 95	[120]
Pd-based membrane	19	87	95	550	92	[121]
PCMR	25	99.9	98	800	99	[72]

Malerød-Fjeld et al. [72] showed that the reaction heat required to form H_2 from CH_4 and H_2O scales linearly with the production rate. The heat evolved from the galvanic operation of the membrane distributes along the length of the membrane and originates from compression and Joule contributions [72]. The complete reformer plant was simulated as a function of H_2 production rate by changing the applied current in order to evaluate system heat integration (Figure 13).

**Figure 13.** (a) Schematic of the sequential model and (b,c) heat model for the PCMR system investigated by Malerød-Fjeld et al. [72].

Notably, in order to assess the practical implications of PCMR technology, Malerød-Fjeld et al. made a techno-economic analysis, comparing the operating energy costs of PCMR with water electrolysis and SMR (Figure 14). The analysis reveals that PCMR and SMR are the less sensitive technologies to energy prices. The PCMR technology allows significant process intensification. High energy efficiency together with its hybrid nature, which uses 1/3 of electricity and 2/3 of natural gas, decreases the carbon footprint especially when the sources of electricity are renewable energies. Moreover, PCMR can benefit from producing a nearly pure stream of CO_2 , enabling carbon capture, use, and storage for industrial scale H_2 production at locations with access to infrastructure for CO_2 storage and use.

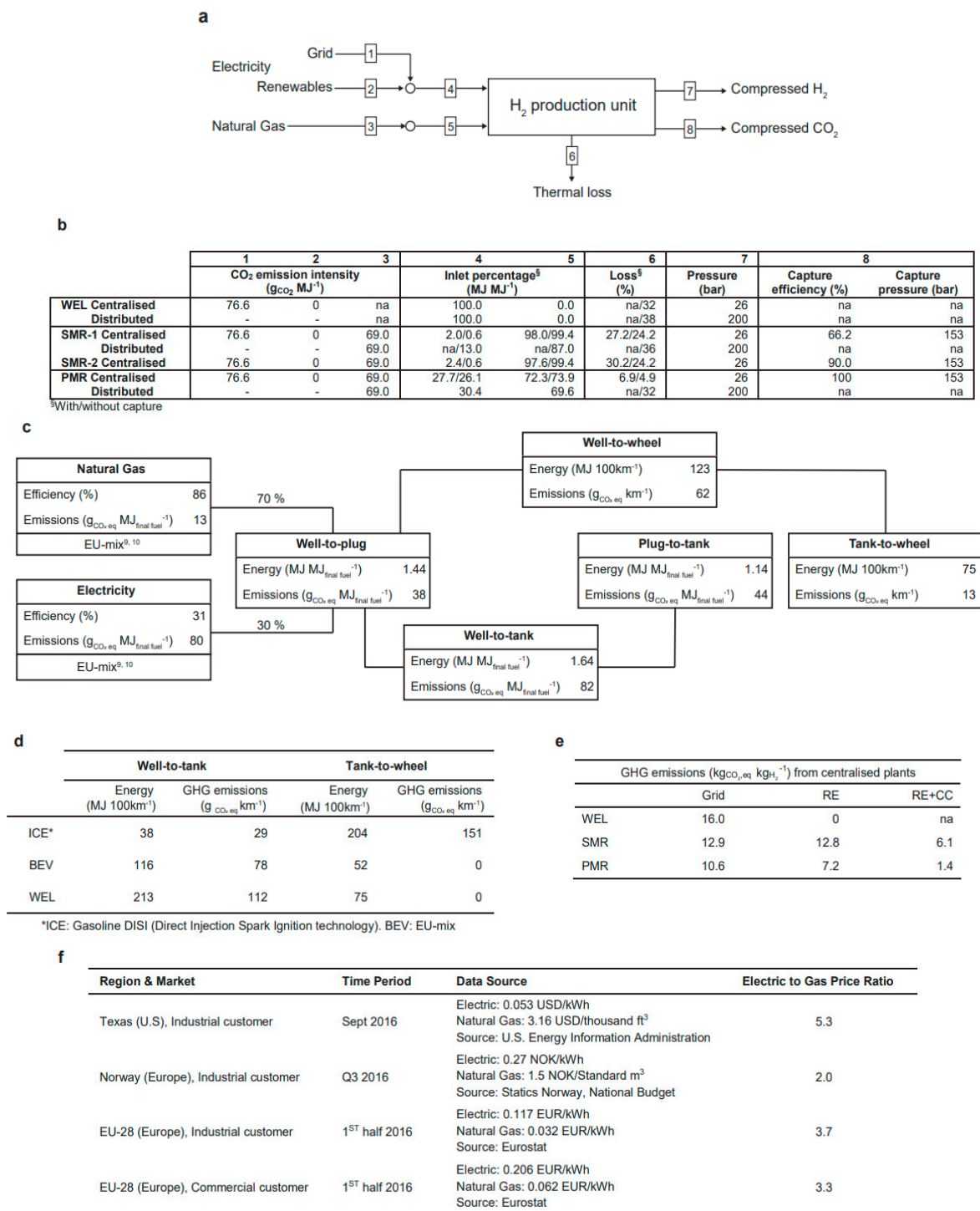


Figure 14. Techno-economic evaluation of PCMR technology investigated by Malerød-Fjeld et al. [72]. (a) Schematic representation of techno-economic evaluation of hydrogen production technologies; (b) summary of inputs and assumptions for the evaluation; (c) schematic representation of well-to-wheel calculation; (d) breakdown of well-to-wheel analysis in terms of efficiencies and GHG emissions for battery electric vehicle (BEV) and internal combustion engine (ICE); (e) GHG emissions of the expended energy for the production of hydrogen in centralised plants using grid electricity, renewable electricity (RE) or RE with carbon capture (RE + CC) for the SMR and PCMR plants; (f) electricity to natural gas price ratio in different regions and markets.

Recently, Clark et al. [115] (Table 4, entry 3) proposed an optimized PCMR which retains the energy efficiency and H₂ recovery of single cells while achieving a 36-fold increase in H₂ production capacity. The PCMR stacks showed high-pressure H₂ at high purity and a CO₂-rich effluent at a hydrogen recovery and methane conversion > 99%. These results are very promising compared to Pd based membrane reformers.

4.2. RePCECs

As reported above, water electrolysis or water splitting via electricity enables energy storage in the H₂ molecule, which can be converted back into electricity through fuel cells or used in chemical processing (Figure 6, above). Among the different types of electrolyzers discussed above, PCECs in which electron flow through the device is accompanied by a flow of protons through a ceramic electrolyte are promising because of the potential for high energy efficiency and the possibility to produce dry pressurized H₂ [122]. RePCECs allow the seasonal energy storage challenge of intermittent renewable electricity generation, favoring the paradigm based on decarbonized heat, to be addressed. Indeed, conventional batteries are less suited for seasonal energy storage due to self-discharge and economic constraints than they are for short-term energy storage [119,123–126]. A RePCEC produces H₂ from water when there is an excess of renewable electricity on the grid that might otherwise go to waste; otherwise, it can work in fuel cell mode using the stored H₂ to produce electricity when there is not enough electricity available on the grid [127]. In particular, in an RePCEC, in the electrolysis (EC) mode, the applied external voltage drives H⁺ from the air electrode to which steam, i.e., H₂O, is fed toward the electrode where H₂ is produced; in the fuel cell mode (FC), electric power is generated as a result of the oxidation of H₂, which is fed to the fuel side of the cell (Figure 15).

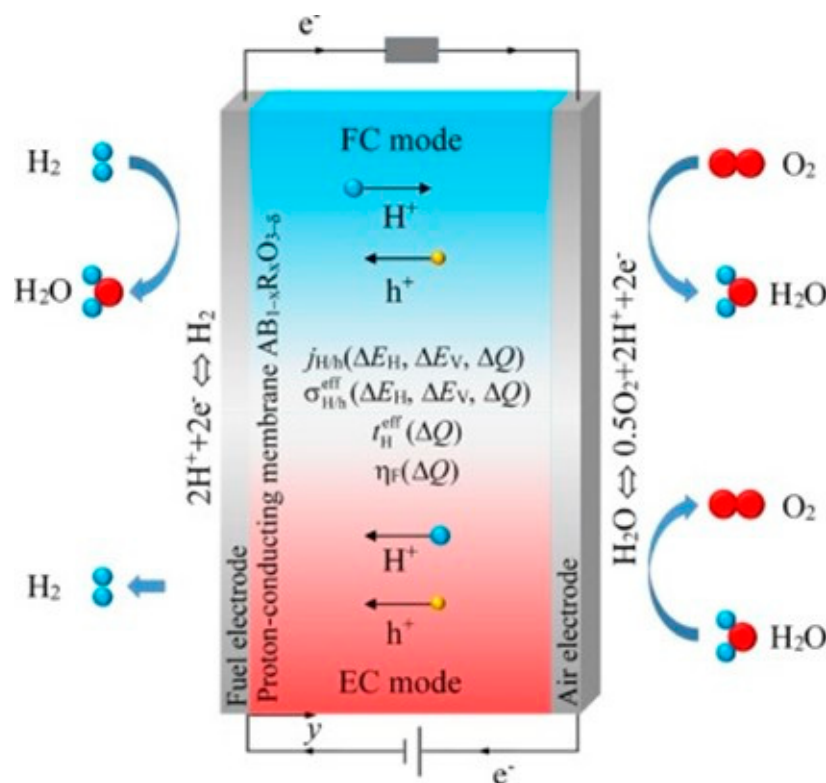


Figure 15. Schematic image of a RePCEC. Reproduced from [128] with permission of Elsevier.

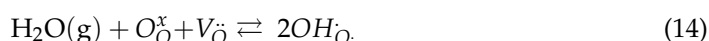
Dailly et al. [76] used BaCe_{0.8}Zr_{0.1}Y_{0.1}O_{3-d} (BCZY81) as a proton conducting ceramic membrane. Several reversible cycles into fuel cell/steam electrolysis were performed with an accelerated electrical degradation observed (+5%/kh under EC and −8%/kh under FC mode over 800 h). However, the authors of this study reported that deeper investigations

in terms of operation protocols and the optimization of cell architecture (in particular the air electrode coating) are needed in order to improve electrical Faradaic efficiency (FE).

In a subsequent study, Duan et al. [75] correlate the poor FE observed in electrolysis mode with the electronic leakage due to minority *p*-type electronic conduction in common proton-conducting ceramic membranes. Indeed, electron holes are produced via the incorporation of molecular oxygen into oxygen vacancies as follows:



Instead, the desired hydroxide defect, OH_{O} , is formed via the incorporation of water into oxygen vacancies via the hydration reaction:



So, a competition between oxidation (Equation (13)) and hydration (Equation (14)) for oxygen vacancies exists [111]. Increasing the favorability of reaction (14) suppresses reaction (13) by simultaneously increasing the proton transference number and decreasing the hole transference number, which in turn decreases electronic leakage. These relationships present the opportunity to tune the composition of proton conducting ceramic membrane and cell operating conditions to achieve higher FE. The equilibrium constant of the hydration reaction (14), i.e., $K_{\text{hydration}}$, can be expressed in terms of thermodynamic parameters [111]:

$$K_{\text{hydration}} = \frac{[\text{OH}_{\text{O}}]^2}{[V_{\text{O}}][\text{O}_{\text{O}}^{\times}]p_{\text{H}_2\text{O}}} = \exp\left(\frac{\Delta S_{\text{hydration}}^{\circ}}{R}\right) \exp\left(-\frac{\Delta H_{\text{hydration}}^{\circ}}{RT}\right) \quad (15)$$

where $\Delta S_{\text{hydration}}^{\circ}$ and $\Delta H_{\text{hydration}}^{\circ}$ are the standard hydration entropy and enthalpy, respectively. Equation 15 correlates proton concentration with hydration thermodynamics and provides a tool for the design of materials with high proton concentration at relatively high temperatures. For ABO_3 -based simple perovskites, prior investigation [129–131] has suggested that $\Delta H_{\text{hydration}}^{\circ}$ is correlated with the electronegativities of the cations, which relate to the basicity of the oxide. At 600 °C, cerates such as barium cerates, i.e., BCY exhibits the largest hydration equilibrium constant, which both favors high proton concentration and suppresses the parasitic oxidation reaction. At the opposite end, the lower $K_{\text{hydration}}$ value observed in zirconates (such as BZY) is the cause of low proton concentration and conductivity, and also of more oxygen vacancies available for oxidation resulting in higher hole concentrations and greater electronic leakage.

The most common proton-conducting ceramic membranes used in RePCECs employ yttrium-doped barium zirconate (BZY), barium cerates (BCY), and solid solutions thereof (BCZY). These ceramic membranes are mixed ionic-electronic conductors and not pure proton conductors. Even though electronic conduction does not greatly affect device performance in fuel cell mode, because transport across the membrane is dominated by protons and oxygen vacancies, in electrolysis mode, electronic conduction transport of delocalized small polarons O_{O} is not negligible. BZY20 and BCZYYb show significantly higher electronic transport with severe electronic leakage in BZY20 more than in BCZYYb, which has a high Ce content at the B site, and therefore lower FE in electrolysis mode. So, the findings by Duan et al. [75] suggest that the preferred ceramic membrane composition for RePCECs and proton-conducting fuel cells (PCFCs) should be different. Indeed, one of the main challenges in the development of RePCECs is to enhance their performance by tailoring the composition of the ceramic membrane acting as electrolyte [111,132]. Putilov and Tsidilkovski [128] investigated theoretically the impact of acceptor-bound states of ionic defects in a proton-conducting oxide with proton and hole conductivity on the performance of protonic ceramic fuel and electrolysis cells operating on humidified hydrogen. The results are presented for the electrochemical cell based on $\text{BaZr}_{0.8}\text{M}_{0.2}\text{O}_{3-\delta}$. Acceptor doping of a proton conducting oxide is necessary to create oxygen vacancies required for

the oxide hydration. To analyze the effect of acceptor doping, Putilov and Tsidilkovski [128] have considered proton hopping over bound and free oxygen sites for two types of potential energy landscape (Q) (Figure 16): (i) $\Delta Q = 0$, which corresponds to a weak effect of acceptor impurities; (ii) $\Delta Q = \Delta E_H$ where ΔE_H is the trapping energy of protons, which represents the situation where impurities considerable reduce both the proton bound-state energy and the saddle point energy for transition between neighboring bound sites.

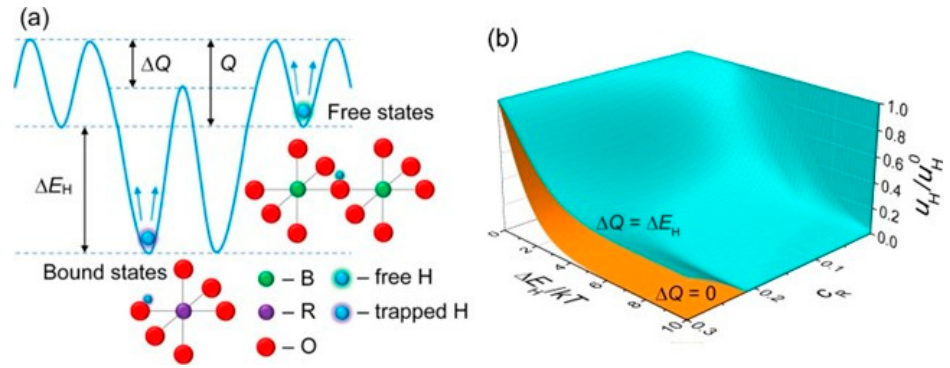


Figure 16. Proton transfer in an acceptor-doped perovskite $AB_{1-x}R_xO_{3-\delta}$. (a) Schematic representation of the potential energy landscape for proton hopping; (b) Proton mobility u_H normalized to μ_H^0 as a function of the proton trapping energy $\Delta E_H/kT$ and dopant content c_R calculated for $\Delta Q = 0$ (lower surface) and $\Delta Q = \Delta E_H$ (upper surface). μ_H^0 is the proton mobility at $\Delta E_H = \Delta E_V = \Delta Q = 0$. Reproduced from [128] with permission of Elsevier.

Fuel cells generate less electric power at a given current, and, conversely, higher applied electric power is required for electrolyzers to maintain the same current when impurities that provide deeper traps for protons and oxygen vacancies are present. Such an effect of acceptor impurities on the power density (P) of a PCEC is shown in Figure 17a, where the values of the power density calculated for Y-, Sc-, Gd- and In-doped $BaZrO_3$ with the corresponding trapping energies of protons (ΔE_H) and vacancies (ΔE_V) are given. It can be observed that the reduction in the P for the considered dopants is minimal for Y-doped $BaZrO_3$ ($\Delta E_H = 0.11$ eV, $\Delta E_V = 0.31$ eV), while for In-doped $BaZrO_3$, the largest power loss ($\Delta E_H = 0.17$ eV, $\Delta E_V = 0.52$ eV) can be obtained. Figure 17b shows U-j and P-j curves at different trapping energies.

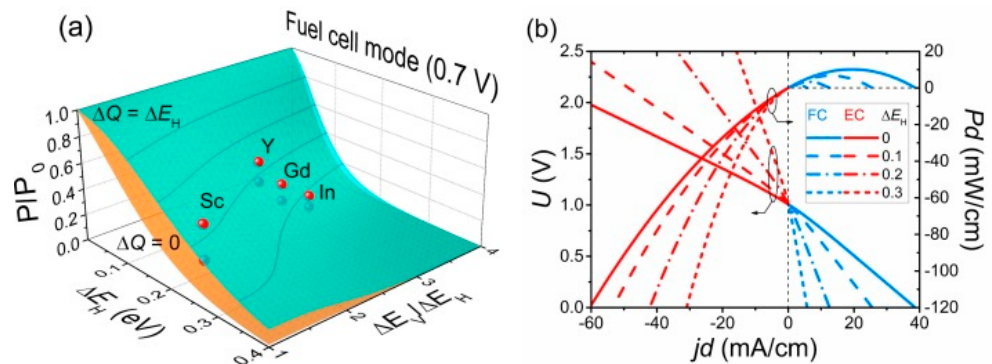


Figure 17. Characteristics of the PCEC operating under humidified H_2 (2% H_2O) and humidified air (50% H_2O) supplied, respectively, to the fuel and air electrodes ($T = 600$ °C). (a) Normalized power density P of the fuel cell as a function of the proton trapping energy ΔE_H and the ratio $\Delta E_V/\Delta E_H$ ($U = 0.7$ V). (b) Cell voltage (left axis) and power density (right axis) versus current density dependences calculated at different trapping energies ΔE_H and ΔE_V for the PCEC operating in the fuel and electrolysis cell modes ($\Delta Q = \Delta E_H$, $\Delta E_V/\Delta E_H = 2$). Reproduced from [128] with permission of Elsevier.

5. Conclusions and Outlook

Proton-conducting ceramic membranes play a relevant role in energy conversion and storage applications including fuel cells for power generation, electrolyzers for hydrogen production, reversible electrochemical cells for long-term energy storage, electrochemical cells/membrane reactors for natural gas conversion. In particular, among the types of reactors for extracting hydrogen from natural gas, electrochemical membrane reactors based on proton ceramic membranes offer a promising opportunity for sustainable industrial growth, possessing unique characteristics such as 100% selectivity gas separation avoiding high pressures at the membrane upper stream, facilitating the use of joule heating instead of thermal heating based on fossil fuels. However, despite their potential in various fields, commercialization of proton conducting ceramic membranes remains a challenge: their performance and stability should be improved and large-scale membrane fabrication strategies are needed. To address such challenges, some key points should be considered:

- (i). The defect chemistry and transport properties of proton-conducting ceramic membranes and positive electrode materials as well as the relationship of defect chemistry and transport properties of these materials with composition, stoichiometry, microstructure, and operating conditions.
- (ii). The design of positive electrodes for PCECs and RePCECs to enhance bulk proton conductivity.
- (iii). The development of appropriate catalysts with specific activities for natural gas reforming and compatibility with other components of protonic ceramic devices.
- (iv). The engineering of the interface between the catalyst and the negative electrode to tune the electrochemical reactions.

Funding: This research received no external funding.

Data Availability Statement: Not applicable.

Conflicts of Interest: The authors declare no conflict of interest.

References

1. World Energy Transitions Outlook: 1.5 °C, Irena. 2022. Available online: <https://www.irena.org/Publications/2023/Jun/World-Energy-Transitions-Outlook-2023#:~:text=IRENA\T1\textquoterights%201.5%C2%B0C%20Scenario,clean%20hydrogen%20and%20sustainable%20biomass> (accessed on 18 August 2023).
2. Li, S.; Zhang, H.; Nie, J.; Dewil, R.; Baeyens, J.; Deng, Y. The Direct Reduction of Iron Ore with Hydrogen. *Sustainability* **2021**, *13*, 8866. [CrossRef]
3. Li, S.; Kang, Q.; Baeyens, J.; Zhang, H.L.; Deng, Y.M. Hydrogen Production: State of Technology. *IOP Conf. Ser. Earth Environ. Sci.* **2020**, *544*, 012011. [CrossRef]
4. Baeyens, J.; Zhang, H.; Nie, J.; Appels, L.; Dewil, R.; Ansart, R.; Deng, Y. Reviewing the potential of bio-hydrogen production by fermentation. *Renew. Sustain. Energy Rev.* **2020**, *131*, 110023. [CrossRef]
5. Chao, C.; Deng, Y.; Dewil, R.; Baeyens, J.; Fan, X. Post-combustion carbon capture. *Renew. Sustain. Energy Rev.* **2021**, *138*, 110490. [CrossRef]
6. Schiffer, Z.J.; Manthiram, K. Electrification and Decarbonization of the Chemical Industry. *Joule* **2017**, *1*, 10–14. [CrossRef]
7. Henry, A.; Prasher, R.; Majumdar, A. Five thermal energy grand challenges for decarbonization. *Nat. Energy* **2020**, *5*, 635–637. [CrossRef]
8. Rightor, E.; Whitlock, A.; Elliott, R.N. *Beneficial Electrification in Industry*; Research Report; American Council for an Energy-Efficient Economy: Washington, DC, USA, 2020.
9. Savut, I. Industrial Heat: Deep Decarbonization Opportunities. *Bloomberg New Energy Finance*, 2019.
10. Global Carbon Project. Supplemental Data of Global Carbon Budget 2019 (Version 1.0) [Data Set]. Available online: <https://www.icos-cp.eu/science-and-impact/global-carbon-budget/2019> (accessed on 18 August 2023). [CrossRef]
11. Thiel, G.P.; Stark, A.K. To decarbonize industry, we must decarbonize heat. *Joule* **2021**, *5*, 531–550. [CrossRef]
12. Colbertaldo, P.; Guandalini, G.; Campanari, S. Modelling the Integrated Power and Transport Energy System: The Role of Power-To-Gas and Hydrogen in Long-Term Scenarios for Italy. *Energy* **2018**, *154*, 592–601. [CrossRef]
13. Buonomenna, M.G. *Nano-Enhanced and Nanostructured Polymer-Based Membranes for Energy Applications*, 1st ed.; Woodhead Publishing: Sawston, UK, 2022.
14. Atwell, C. 6 Promising Energy Storage Options to Tie to the Grid. *Power Electronics*. 2018. Available online: <https://www.electronicdesign.com/technologies/power/alternative-energy/article/21199504/6-promising-energy-storage-options-to-tie-into-the-grid> (accessed on 18 August 2023).

15. Deng, Y.; Li, S.; Dewil, R.; Appels, L.; Yang, M.; Zhang, H.; Baeyens, J. Water splitting by $\text{MnFe}_2\text{O}_4/\text{Na}_2\text{CO}_3$ reversible redox reactions. *RSC Adv.* **2022**, *12*, 31392–31401. [CrossRef]
16. Deng, Y.; Dewil, R.; Appels, L.; Li, S.; Baeyens, J.; Degève, J.; Wang, G. Thermo-chemical water splitting: Selection of priority reversible redox reactions by multi-attribute decision making. *Renew. Energy* **2021**, *170*, 800–810. [CrossRef]
17. Safari, F.; Dincer, I. A review and comparative evaluation of thermochemical water splitting cycles for hydrogen production. *Energy Convers. Manag.* **2020**, *205*, 112182. [CrossRef]
18. Available online: <https://www.nationalgrid.com/stories/energy-explained/hydrogen-colour-spectrum#:~:text=Blue%20hydrogen%20is%20produced%20mainly,produced%20as%20a%20by%2Dproduct> (accessed on 18 August 2023).
19. Sandalow, D.; Friedmann, J.; Aines, R.; McCormick, C.; McCoy, S.; Stolaroff, J. *ICEF Industrial Heat Decarbonization Roadmap*; ICEF (Innovation for Cool Earth Forum): Tokyo, Japan, 2019.
20. Rostrup-Nielsen, J.; Christiansen, L.J. *Concepts in Syngas Manufacture*; Imperial College Press: London, UK, 2011.
21. Kumar, A.; Baldea, M.; Edgar, T.F. A Physics-Based Model for Industrial Steam-Methane Reformer Optimization with Non-Uniform Temperature Field. *Comput. Chem. Eng.* **2017**, *105*, 224–236. [CrossRef]
22. Latham, D.A.; McAuley, K.B.; Peppley, B.A.; Raybold, T.M. Mathematical Modeling of an Industrial Steam-Methane Reformer for on-Line Deployment. *Fuel Process. Technol.* **2011**, *92*, 1574–1586. [CrossRef]
23. Gallucci, F.; Fernandez, E.; Corengia, P.; van Sint Annaland, M. Recent advances on membranes and membrane reactors for hydrogen production. *Chem. Eng. Sci.* **2013**, *92*, 40–66. [CrossRef]
24. Wismann, S.T.; Engbæk, J.S.; Vendelbo, S.B.; Eriksen, W.L.; Frandsen, C.; Mortensen, P.M.; Chorkendorff, I. Electrified methane reforming: Elucidating transient phenomena. *Chem. Eng. J.* **2021**, *425*, 131509. [CrossRef]
25. Le Qu'ère, N.; Moriarty, C.; Andrew, R.; Peters, R.M.; Ciaia, G.P.; Friedlingstein, P.; Jones, S.D.; Sitch, S.; Tans, P.; Arneeth, A.; et al. Global Carbon Budget 2018. *Earth Syst. Sci. Data.* **2018**, *10*, 2141–2194. [CrossRef]
26. Wismann, S.T.; Engbæk, J.S.; Vendelbo, S.B.; Bendixen, F.B.; Eriksen, W.L.; Aasberg-petersen, K.; Frandsen, C.; Chorkendorff, I.; Mortensen, P.M. Electrified methane reforming: A compact approach to greener industrial hydrogen production. *Science* **2019**, *364*, 756–759.
27. Almind, M.R.; Vendelbo, S.B.; Hansen, M.F.; Vinumd, M.G.; Frandsen, C.; Mortensen, P.M.; Engbæk, J.S. Improving performance of induction-heated steam methane reforming. *Catal. Today* **2020**, *342*, 13–20. [CrossRef]
28. Available online: https://energiforskning.dk/sites/energiforskning.dk/files/slutrappporter/induction_heated_hydrogen_production_-_eudp_project_no_64013-0511_-_final_report.pdf (accessed on 18 August 2023).
29. Scarfiello, C.; Bellusci, M.; Pilloni, L.; Pietrogiaconi, D.; La Barbera, A.; Varsano, F. Supported catalysts for induction-heated steam reforming of methane. *Int. J. Hydrog. Energy* **2021**, *46*, 134–145. [CrossRef]
30. Wismann, S.T.; Engbæk, J.S.; Vendelbo, S.B.; Eriksen, W.L.; Frandsen, C.; Mortensen, P.M.; Chorkendorff, I. Electrified Methane Reforming: Understanding the Dynamic Interplay. *Ind. Eng. Chem. Res.* **2019**, *58*, 23380–23388. [CrossRef]
31. Ambrosetti, M.; Beretta, A.; Groppi, G.; Tronconi, E. A Numerical Investigation of Electrically-Heated Methane Steam Reforming Over Structured Catalysts. *Front. Chem. Eng.* **2021**, *3*, 747636. [CrossRef]
32. Lu, Y.R.; Nikrityuk, P.A. Steam methane reforming driven by the Joule heating. *Chem. Eng. Sci.* **2022**, *251*, 117446. [CrossRef]
33. Zheng, L.; Ambrosetti, M.; Marangoni, D.; Beretta, A.; Groppi, G.; Tronconi, E. Electrified methane steam reforming on a washcoated SiSiC foam for low-carbon hydrogen production. *AIChE J.* **2023**, *69*, e17620. [CrossRef] [PubMed]
34. Feng, J.; Sun, X.; Li, Z.; Hao, X.; Fan, M.; Ning, P.; Li, K. Plasma-Assisted Reforming of Methane. *Adv. Sci.* **2022**, *9*, 2203221. [CrossRef]
35. Dinh, D.K.; Trenchev, G.; Lee, D.H.; Bogaerts, A. Arc Plasma Reactor Modification for Enhancing Performance of Dry Reforming of Methane. *J. CO₂ Util.* **2020**, *42*, 101352. [CrossRef]
36. Pérez-Camacho, M.N.; Abu-Dahrieh, J.; Rooney, D.; Sun, K. Biogas Reforming Using Renewable Wind Energy and Induction Heating. *Catal. Today* **2015**, *242*, 129–138. [CrossRef]
37. de Dios García, I.; Stankiewicz, A.; Nigar, H. Syngas Production via Microwave-Assisted Dry Reforming of Methane. *Catal. Today* **2021**, *362*, 72–80. [CrossRef]
38. Palma, V.; Barba, D.; Cortese, M.; Martino, M.; Renda, S.; Meloni, E. Microwaves and Heterogeneous Catalysis: A Review on Selected Catalytic Processes. *Catalysts* **2020**, *10*, 246. [CrossRef]
39. Heijkers, S.; Aghaei, M.; Bogaerts, A. Plasma-Based CH₄ Conversion into Higher Hydrocarbons and H₂: Modeling to Reveal the Reaction Mechanisms of Different Plasma Sources. *J. Phys. Chem. C Nanomater. Interfaces* **2020**, *124*, 7016–7030. [CrossRef] [PubMed]
40. Zheng, L.; Ambrosetti, M.; Beretta, A.; Groppi, G.; Tronconi, E. Electrified CO₂ valorization driven by direct Joule heating of catalytic cellular substrates. *Chem. Eng. J.* **2023**, *466*, 143154. [CrossRef]
41. Dou, L.; Yan, C.; Zhong, L.; Zhang, D.; Zhang, J.; Li, X.; Xiao, L. Enhancing CO₂ Methanation over a Metal Foam Structured Catalyst by Electric Internal Heating. *Chem. Commun.* **2020**, *56*, 205–208. [CrossRef]
42. Badakhsh, A.; Kwak, Y.; Lee, Y.-J.; Jeong, H.; Kim, Y.; Sohn, H.; Nam, S.W.; Yoon, C.W.; Park, C.W.; Jo, Y.S. A Compact Catalytic Foam Reactor for Decomposition of Ammonia by the Joule-Heating Mechanism. *Chem. Eng. J.* **2021**, *426*, 130802. [CrossRef]
43. Gorky, F.; Lucero, J.M.; Crawford, J.M.; Blake, B.A.; Guthrie, S.; Carreon, M.A.; Carreon, M.L. Insights on cold plasma ammonia synthesis and decomposition using alkaline earth metal-based perovskites. *Catal. Sci. Technol.* **2021**, *11*, 5109–5118. [CrossRef]

44. Andersen, J.A.; Christensen, J.M.; Østberg, M.; Bogaerts, A.; Jensen, A.D. Plasma-catalytic ammonia decomposition using a packed-bed dielectric barrier discharge reactor. *Int. J. Hydrogen Energy* **2022**, *47*, 32081–32091. [[CrossRef](#)]
45. Seyfeli, R.C.; Varisli, D. Performance of microwave reactor system in decomposition of ammonia using nickel based catalysts with different supports. *Int. J. Hydrogen Energy* **2022**, *47*, 15175–15188. [[CrossRef](#)]
46. Microwave-enhanced catalytic ammonia synthesis under moderate pressure and temperature. *Catal. Commun.* **2021**, *159*, 106344. [[CrossRef](#)]
47. Miller, H.A.; Bouzek, K.; Hnat, J.; Loos, S.; Bernacker, C.I.; Weißgarber, T.; Rontzsch, L.; Meier-Haack, J. Green hydrogen from anion exchange membrane water electrolysis: A review of recent developments in critical materials and operating conditions. *Sustain. Energy Fuels* **2020**, *4*, 2114–2133. [[CrossRef](#)]
48. Ebbesen, S.D.; Jensen, S.H.; Hauch, A.; Mogensen, M.B. High temperature electrolysis in alkaline cells, solid proton conducting cells, and solid oxide cells. *Chem. Rev.* **2014**, *114*, 10697–10734. [[CrossRef](#)] [[PubMed](#)]
49. Zhang, W.; Liu, M.; Gu, X.; Shi, Y.; Deng, Z.; Ca, N. Water Electrolysis toward Elevated Temperature: Advances, Challenges and Frontiers. *Chem. Rev.* **2023**, *123*, 7119–7192. [[CrossRef](#)] [[PubMed](#)]
50. Buonomenna, M.G. Membrane processes for a sustainable industrial growth. *RSC Adv.* **2013**, *3*, 5694–5740. [[CrossRef](#)]
51. Noble, R.D.; Stern, S.A. Membrane separations technology: Principles and applications. In *Membrane Science and Technology*; Elsevier Science: Amsterdam, The Netherlands, 1995.
52. Kluiters, S.C.A. *Energy Research Centre of The Netherlands*; TNO: Petten, The Netherlands, 2004.
53. Ivanova, M.E.; Escolástico, S.; Balaguer, M.; Palisaitis, J.; Sohn, Y.J.; Meulenberg, W.A.; Guillon, O.; Mayer, J.; Serra, J.M. Hydrogen separation through tailored dual phase membranes with nominal composition $\text{BaCe}_{0.8}\text{Eu}_{0.2}\text{O}_{3-\delta}\cdot\text{Ce}_{0.8}\text{Y}_{0.2}\text{O}_{2-\delta}$ at intermediate temperatures. *Sci. Rep.* **2016**, *6*, 34773. [[CrossRef](#)]
54. Phair, J.W.; Badwal, S.P.S. Review of proton conductors for hydrogen separation. *Ionics* **2006**, *12*, 103–115. [[CrossRef](#)]
55. Norby, T.; Larring, Y. Mixed hydrogen ion-electronic conductors for hydrogen permeable membranes. *Solid. State Ion.* **2000**, *136*, 139–148. [[CrossRef](#)]
56. Jaffe, B.; Cook, W.R.; Jaffe, H. *Piezoelectric Ceramics*; Academic Press: London, UK; New York, NY, USA, 1971.
57. Esquirol, A.; Kilner, J.; Brandon, N. Oxygen transport in $\text{La}_{0.6}\text{Sr}_{0.4}\text{Co}_{0.2}\text{Fe}_{0.8}\text{O}_{3\text{d}}/\text{Ce}_{0.8}\text{Ge}_{0.2}\text{O}_{2\text{x}}$ composite cathode for ITSOFCs. *Solid. State Ion.* **2004**, *175*, 63–67. [[CrossRef](#)]
58. Uchida, H.; Maeda, N.; Iwahara, H. Relation between proton and hole conduction in SrCeO_3 -based solid electrolytes under water-containing atmospheres at high temperatures. *Solid. State Ion.* **1983**, *11*, 117–124. [[CrossRef](#)]
59. Iwahara, H.; Yajima, T.; Hibino, T.; Ushida, H. Performance of solid oxide fuel cell using proton and oxide ion mixed conductors based on $\text{BaCe}_{1\text{x}}\text{Sm}_\text{x}\text{O}_{3\text{d}}$. *J. Electrochem. Soc.* **1993**, *140*, 1687–1691. [[CrossRef](#)]
60. Bonanos, N.; Knight, K.S.; Ellis, B. Perovskite solid electrolytes: Structure, transport properties and fuel cell applications. *Solid. State Ion.* **1995**, *79*, 161–170. [[CrossRef](#)]
61. Papac, M.; Stevanović, V.; Zakutayev, A.; O’Hayre, R. Triple ionic-electronic conducting oxides for next-generation electrochemical devices. *Nat. Mater.* **2021**, *20*, 301–313. [[CrossRef](#)]
62. Hamakaw, S.; Li, L.; Li, A.W.; Iglesia, E. Interdiffusion in alkali ion sorption by hydrous stannic oxide: Mechanism and effect of co-ion. *Solid. State Ion.* **2002**, *48*, 71–77.
63. Matsumoto, H.; Shimura, T.; Iwahara, H.; Higuchi, T.; Yashiro, K.; Kaimai, A.; Kawada, T.; Mizusaki, J. Hydrogen separation using proton-conducting perovskites. *J. Alloys Compd.* **2006**, *408–412*, 456–462. [[CrossRef](#)]
64. Matsumoto, H.; Okada, S.; Hashimoto, S.; Sasaki, K.; Yamamoto, R.; Enoki, M.; Ishihara, T. Hydrogen separation from syngas using high temperature proton conductors. *Ionics* **2007**, *13*, 93–99. [[CrossRef](#)]
65. Fang, S.M.; Bi, L.; Yang, C.L.; Yan, L.T.; Chen, C.S.; Liu, W. H_2S poisoning and regeneration of $\text{Ni-BaZr}_{0.1}\text{Ce}_{0.7}\text{Y}_{0.2}\text{O}_{3\text{d}}$ at intermediate temperature. *J. Alloys Compd.* **2009**, *475*, 935–939. [[CrossRef](#)]
66. Fabbri, E.; Bi, L.; Pergolesi, D.; Traversa, E. Towards the next generation of solid oxide fuel cells operating below 600 c with chemically stable proton-conducting electrolytes. *Adv. Mater.* **2012**, *24*, 195–208. [[CrossRef](#)] [[PubMed](#)]
67. Tao, Z.; Yan, L.; Qiao, J.; Wang, B.; Zhang, L.; Zhang, J. A review of advanced proton-conducting materials for hydrogen separation. *Prog. Mater. Sci.* **2015**, *74*, 1–50. [[CrossRef](#)]
68. KQin, G.; Bao, J.; Ruan, F.; An, S.; Wang, Z.; Li, L. Enhanced grain boundary conductivity of Gd and Sc co-doping BaZrO_3 proton conductor for proton ceramic fuel cell. *Chem. Eng. J.* **2023**, *466*, 143114.
69. Shirpour, M.; Merkle, R.; Maier, J. Evidence for space charge effects in Y-doped BaZrO_3 from reduction experiments. *Solid. State Ion.* **2012**, *216*, 1–5. [[CrossRef](#)]
70. Morejudo, S.H.; Zanon, R.; Escolastico, S.; Yuste-Tirados, I.; Malerød-Fjeld, H.; Vestre, P.K.; Coors, W.G.; Martí ´nez, A.; Norby, T.; Serra, J.M.; et al. Direct conversion of methane to aromatics in a catalytic co-ionic membrane reactor. *Science* **2016**, *353*, 563–566. [[CrossRef](#)] [[PubMed](#)]
71. Ding, D.; Zhang, Y.; Wu, W.; Chen, D.; Liu, M.; He, T. A novel low thermal-budget approach for the co-production of ethylene and hydrogen via the electrochemical non-oxidative deprotonation of ethane. *Energy Environ. Sci.* **2018**, *11*, 1710–1716. [[CrossRef](#)]
72. Malerød-Fjeld, H.; Clark, D.; Yuste-Tirados, I.; Zanon, R.; Catalan-Martinez, D.; Beeaff, D.; Morejudo, S.H.; Vestre, P.K.; Norby, T.; Haugsrud, R.; et al. Thermo-electrochemical production of compressed hydrogen from methane with near-zero energy loss. *Nat. Energy* **2017**, *2*, 923–931. [[CrossRef](#)]

73. Deibert, W.; Ivanova, M.E.; Baumann, S.; Guillon, O.; Meulenberg, W.A. Ion-conducting ceramic membrane reactors for high-temperature applications. *J. Membr. Sci.* **2017**, *543*, 79–97. [[CrossRef](#)]
74. Kyriakou, V.; Garagounis, I.; Vourros, A.; Vasileiou, E.; Manerbino, A.; Coors, W.G.; Stoukides, M. Methane steam reforming at low temperatures in a $\text{BaZr}_{0.7}\text{Ce}_{0.2}\text{Y}_{0.1}\text{O}_{2.9}$ proton conducting membrane reactor. *Appl. Catal. B Environ.* **2016**, *186*, 1–9. [[CrossRef](#)]
75. Duan, C.; Kee, R.; Zhu, H.; Sullivan, N.; Zhu, L.; Bian, L.; Jennings, D.; O'Hayre, R. Highly efficient reversible protonic ceramic electrochemical cells for power generation and fuel production. *Nat. Energy* **2019**, *4*, 230–240. [[CrossRef](#)]
76. Dailly, J.; Ancelin, M.; Marrony, M. Long term testing of BCZY-based protonic ceramic fuel cell PCFC: Micro-generation profile and reversible production of hydrogen and electricity. *Solid. State Ion.* **2017**, *306*, 69–75. [[CrossRef](#)]
77. Chen, Y.; Liao, Q.; Li, Z.; Wang, H.H.; Wei, Y.Y.; Feldhoff, A.; Caro, J. A CO_2 -stable hollow-fiber membrane with high hydrogen permeation flux. *AIChE J.* **2015**, *61*, 1997–2007. [[CrossRef](#)]
78. Elangovan, S.; Nair, B.G.; Small, T.A. Ceramic Mixed Protonic/Electronic Conducting Membranes for Hydrogen Separation. U.S. Patent US7258820B2, 21 August 2007.
79. Matsumoto, H.; Shimura, T.; Higuchi, T.; Tanaka, H.; Katahira, K.; Otake, T.; Kudo, T.; Yashiro, K.; Kaimai, A.; Kawada, T.; et al. Protonic-electronic mixed conduction and hydrogen permeation in $\text{BaCe}_{0.9-x}\text{Y}_{0.1}\text{Ru}_x\text{O}_{3-\alpha}$. *J. Electrochem. Soc.* **2005**, *152*, A488–A492. [[CrossRef](#)]
80. Cai, M.; Liu, S.; Efimov, K.; Caro, J.; Feldhoff, A.; Wang, H. Preparation and hydrogen permeation of $\text{BaCe}_{0.95}\text{Nd}_{0.05}\text{O}_{3-\delta}$ membranes. *J. Membr. Sci.* **2009**, *343*, 90–96. [[CrossRef](#)]
81. Escolástico, S.; Ivanova, M.; Solís, C.; Roitsch, S.; Meulenberg, W.A.; Serra, J.M. Improvement of transport properties and hydrogen permeation of chemically-stable proton-conducting oxides based on the system $\text{BaZr}_{1-x-y}\text{Y}_x\text{M}_y\text{O}_{3-\delta}$. *RSC Adv.* **2012**, *2*, 4932–4943. [[CrossRef](#)]
82. Cheng, S.G.; Gupta, V.K.; Lin, J.Y.S. Synthesis and hydrogen permeation properties of asymmetric proton-conducting ceramic membranes. *Solid. State Ion.* **2005**, *176*, 2653–2662. [[CrossRef](#)]
83. Qi, X.W.; Lin, Y.S. Electrical conduction and hydrogen permeation through mixed proton-electron conducting strontium cerate membranes. *Solid. State Ion.* **2000**, *130*, 149–156. [[CrossRef](#)]
84. Kniep, J.; Lin, Y.S. Effect of Zirconium Doping on Hydrogen Permeation through Strontium Cerate Membranes. *Ind. Eng. Chem. Res.* **2010**, *49*, 2768–2774. [[CrossRef](#)]
85. Wei, X.; Kniep, J.; Lin, Y.S. Hydrogen permeation through terbium doped strontium cerate membranes enabled by presence of reducing gas in the downstream. *J. Membr. Sci.* **2009**, *345*, 201–206. [[CrossRef](#)]
86. Zhan, S.; Zhu, X.; Ji, B.; Wang, W.; Zhang, X.; Wang, J.; Yang, W.; Lin, L. Preparation and hydrogen permeation of $\text{SrCe}_{0.95}\text{Y}_{0.05}\text{O}_{3-\delta}$ asymmetrical membranes. *J. Membr. Sci.* **2009**, *340*, 241–248. [[CrossRef](#)]
87. Hamakawa, S.; Li, L.; Li, A.; Iglesia, E. Synthesis and hydrogen permeation properties of membranes based on dense $\text{SrCe}_{0.95}\text{Yb}_{0.05}\text{O}_{3-\alpha}$ thin films. *Solid. State Ion.* **2002**, *148*, 71–81. [[CrossRef](#)]
88. Song, S.J.; Wachsmann, E.D.; Rhodes, J.; Dorris, S.E.; Balachandran, U. Hydrogen permeability of $\text{SrCe}_{1-x}\text{M}_x\text{O}_{3-\delta}$ ($x = 0.05$, $M = \text{Eu}$, Sm). *Solid. State Ion.* **2004**, *167*, 99–105. [[CrossRef](#)]
89. Liang, J.; Mao, L.; Li, L.; Yuan, W. Protonic and Electronic Conductivities and Hydrogen Permeation of $\text{SrCe}_{0.95-x}\text{Zr}_x\text{Tm}_{0.05}\text{O}_{3-\delta}$ ($0 < x \leq 0.40$) Membrane. *Chin. J. Chem. Eng.* **2010**, *18*, 506–510.
90. Xing, W.; Dahl, P.I.; Roaas, L.V.; Fontaine, M.L.; Larring, Y.; Henriksen, P.P.; Bredesen, R. Hydrogen permeability of $\text{SrCe}_{0.7}\text{Zr}_{0.25}\text{Ln}_{0.05}\text{O}_{3-\delta}$ membranes ($\text{Ln} = \text{Tm}$ and Yb). *J. Membr. Sci.* **2015**, *473*, 327–332. [[CrossRef](#)]
91. Oh, T.; Yoon, H.; Li, J.; Wachsmann, E.D. Hydrogen permeation through thin supported $\text{SrZr}_{0.2}\text{Ce}_{0.8-x}\text{Eu}_x\text{O}_{3-\delta}$ membranes. *J. Membr. Sci.* **2009**, *345*, 1–4. [[CrossRef](#)]
92. Escolastico, S.; Seeger, J.; Roitsch, S.; Ivanova, M.; Meulenberg, W.A.; Serra, J.M. Enhanced H_2 separation through mixed proton-electron conducting membranes based on $\text{La}_{5.5}\text{W}_{0.8}\text{M}_{0.2}\text{O}_{11.25-\delta}$. *ChemSusChem* **2013**, *6*, 1523–1532. [[CrossRef](#)]
93. Escolastico, S.; Vert, V.B.; Serra, J.M. Preparation and Characterization of Nanocrystalline Mixed Proton-Electronic Conducting Materials Based on the System $\text{Ln}_6\text{WO}_{12}$. *Chem. Mater.* **2009**, *21*, 3079–3089. [[CrossRef](#)]
94. Escolastico, S.; Solís, C.; Serra, J.M. Hydrogen separation and stability study of ceramic membranes based on the system $\text{Nd}_5\text{LnWO}_{12}$. *Int. J. Hydrogen Energ.* **2011**, *36*, 11946–11954. [[CrossRef](#)]
95. Escolastico, S.; Solís, C.; Serra, J.M. Study of hydrogen permeation in $(\text{La}_{5/6}\text{Nd}_{1/6})_{5.5}\text{WO}_{12-\delta}$ membranes. *Solid. State Ion.* **2012**, *216*, 31–35. [[CrossRef](#)]
96. Escolastico, S.; Somacescu, S.; Serra, J.M. Tailoring mixed ionic-electronic conduction in H_2 permeable membranes based on the system $\text{Nd}_{5.5}\text{W}_{1-x}\text{Mo}_x\text{O}_{11.25-\sigma}$. *J. Mater. Chem. A* **2015**, *3*, 719–731. [[CrossRef](#)]
97. Escolastico, S.; Somacescu, S.; Serra, J.M. Solid State Transport and Hydrogen Permeation in the System $\text{Nd}_{5.5}\text{W}_{1-x}\text{Re}_x\text{O}_{11.25-\delta}$. *Chem. Mater.* **2014**, *26*, 982–992. [[CrossRef](#)]
98. Escolastico, S.; Solís, C.; Kjolseth, C.; Serra, J.M. Outstanding hydrogen permeation through CO_2 -stable dual-phase ceramic membranes. *Energ. Environ. Sci.* **2014**, *7*, 3736–3746. [[CrossRef](#)]
99. Rosensteel, W.A.; Ricote, S.; Sullivan, N.P. Hydrogen permeation through dense $\text{BaCe}_{0.8}\text{Y}_{0.2}\text{O}_{3-\delta}$ — $\text{Ce}_{0.8}\text{Y}_{0.2}\text{O}_{2-\delta}$ composite-ceramic hydrogen separation membranes. *Int. J. Hydrogen Energ.* **2016**, *41*, 2598–2606. [[CrossRef](#)]
100. Rebollo, E.; Mortalo, C.; Escolástico, S.; Boldrini, S.; Barison, S.; Serrab, J.M.; Fabrizio, M. Exceptional hydrogen permeation of all-ceramic composite robust membranes based on $\text{BaCe}_{0.65}\text{Zr}_{0.20}\text{Y}_{0.15}\text{O}_{3-\delta}$ and Y- or Gd-doped ceria. *Energ. Environ. Sci.* **2015**, *8*, 3675–3686. [[CrossRef](#)]

101. Fish, J.S.; Ricote, S.; O'Hayre, R.; Bonanos, N. Electrical properties and flux performance of composite ceramic hydrogen separation membranes. *J. Mater. Chem. A* **2015**, *3*, 5392–5401. [[CrossRef](#)]
102. Unemoto, A.; Kaimai, A.; Sato, K.; Yashiro, K.; Matsumoto, H.; Mizusaki, J.; Amezawa, K.; Kawada, T. Hydrogen permeability and electrical properties in oxide composites. *Solid. State Ion.* **2008**, *178*, 1663–1667. [[CrossRef](#)]
103. Meng, X.; Song, J.; Yang, N.; Meng, B.; Tan, X.; Ma, Z.F.; Li, K. Ni-BaCe_{0.95}Tb_{0.05}O_{3-δ} cermet membranes for hydrogen permeation. *J. Membr. Sci.* **2012**, *401*, 300–305. [[CrossRef](#)]
104. Kim, H.; Kim, B.; Lee, J.; Ahn, K.; Kim, H.R.; Yoon, K.J.; Kim, B.K.; Cho, Y.W.; Lee, H.W.; Lee, J.H. Microstructural adjustment of Ni-BaCe_{0.9}Y_{0.1}O_{3-δ} cermet membrane for improved hydrogen permeation. *Ceram. Int.* **2014**, *40*, 4117–4126. [[CrossRef](#)]
105. Song, S.J.; Moon, J.H.; Lee, T.H.; Dorris, S.E.; Balachandran, U. Thickness dependence of hydrogen permeability for NiBaCe_{0.8}Y_{0.2}O_{3-δ}. *Solid. State Ion.* **2008**, *179*, 1854–1857. [[CrossRef](#)]
106. Wei, Y.; Xue, J.; Fang, W.; Chen, Y.; Wang, H.; Caro, J. Enhanced stability of Zr-doped Ba(CeTb)O_{3-δ}-Ni cermet membrane for hydrogen separation. *Chem. Comm.* **2015**, *51*, 11619–11621. [[CrossRef](#)]
107. Zuo, C.; Dorris, S.E.; Balachandran, U.; Liu, M. Effect of Zr-doping on the chemical stability and hydrogen permeation of the NiBaCe_{0.8}Y_{0.2}O_{3-α} mixed protonic-electronic conductor. *Chem. Mater.* **2006**, *18*, 4647–4650. [[CrossRef](#)]
108. Fang, S.; Brinkman, K.S.; Chen, F. Hydrogen permeability and chemical stability of Ni-BaZr_{0.1}Ce_{0.7}Y_{0.1}Yb_{0.1}O_{3-δ} membrane in concentrated H₂O and CO₂. *J. Membr. Sci.* **2014**, *467*, 85–92. [[CrossRef](#)]
109. Fang, S.; Bi, L.; Yan, L.; Sun, W.; Chen, C.; Liu, W. CO₂-Resistant Hydrogen Permeation Membranes Based on Doped Ceria and Nickel. *J. Phys. Chem. C* **2010**, *114*, 10986–10991. [[CrossRef](#)]
110. Balachandran, U.; Lee, T.; Park, C.; Emerson, J.; Picciolo, J.; Dorris, S. Dense cermet membranes for hydrogen separation. *Sep. Purif. Technol.* **2014**, *121*, 54–59. [[CrossRef](#)]
111. Duan, C.; Huang, J.; Sullivan, N.; O'Hayre, R. Proton-conducting oxides for energy conversion and storage. *Appl. Phys. Rev.* **2020**, *7*, 011314. [[CrossRef](#)]
112. Pei, K.; Zhou, Y.; Xu, K.; Zhang, H.; Ding, Y.; Zhao, B.; Yuan, W.; Sasaki, K.; Choi, Y.M. Surface restructuring of a perovskite-type air electrode for reversible protonic ceramic electrochemical cells. *Nat. Commun.* **2022**, *13*, 2207. [[CrossRef](#)]
113. Buonomenna, M.G.; Choi, S.H.; Drioli, E. Catalysis in polymeric membrane reactors: The membrane role. *Asia-Pac. J. Chem. Eng.* **2010**, *5*, 26–34. [[CrossRef](#)]
114. Miachon, S.; Dalmon, J.A. Catalysis in membrane reactors: What about the catalyst? *Top. Catal.* **2004**, *29*, 59–65. [[CrossRef](#)]
115. Clark, D.; Malerød-Fjeld, H.; Budd, M.; Yuste-Tirados, Y.; Beeaff, D.; Aamodt, S.; Nguyen, K.; Ansaloni, L.; Peters, T.; Vestre, P.K.; et al. Single-step hydrogen production from NH₃, CH₄, and biogas in stacked proton ceramic reactors. *Science* **2022**, *376*, 390–393. [[CrossRef](#)] [[PubMed](#)]
116. Basile, A. Hydrogen Production using Pd-based membrane reactors for fuel cells. *Top. Catal.* **2008**, *51*, 107–122. [[CrossRef](#)]
117. Ryu, K.H.; Haile, S. Chemical stability and proton conductivity of doped BaCeO₃-BaZrO₃ solid solutions. *Solid. State Ion.* **1999**, *125*, 355–367. [[CrossRef](#)]
118. Ricote, S.; Bonanos, N.; Caboche, G. Water vapour solubility and conductivity study of the proton conductor BaCe_(0.9-x)Zr_xY_{0.1}O_(3-δ). *Solid. State Ion.* **2009**, *180*, 990–997. [[CrossRef](#)]
119. Yang, L.; Wang, S.; Blinn, K.; Liu, M.; Liu, Z.; Cheng, Z.; Liu, M. Enhanced sulfur and coking tolerance of a mixed ion conductor for SOFCs: BaZr_(0.1)Ce_(0.7)Y_(0.2-x)Yb_(x)O_(3-d). *Science* **2009**, *326*, 126–129. [[CrossRef](#)]
120. Shirasaki, Y.; Tsuneki, T.; Ota, Y.; Yasuda, I.; Tachibana, S.; Nakajima, H.; Kobayashi, K. Development of membrane reformer system for highly efficient hydrogen production from natural gas. *Int. J. Hydrog. Energy* **2009**, *34*, 4482–4487. [[CrossRef](#)]
121. Boeltken, T.; Wunsch, A.; Gietzelt, T.; Pfeifer, P.; Dittmeyer, R. Ultra-compact microstructured methane steam reformer with integrated Palladium membrane for on-site production of pure hydrogen: Experimental demonstration. *Int. J. Hydrog. Energy* **2014**, *39*, 18058–18068. [[CrossRef](#)]
122. Serra, J.M. Electrifying chemistry with protonic cells. *Nat. Energy* **2019**, *4*, 178–179. [[CrossRef](#)]
123. Xu, L.; Jiang, Q.; Xiao, Z.; Li, X.; Huo, J.; Wang, S.; Dai, L. Plasma-engraved Co₃O₄ nanosheets with oxygen vacancies and high surface area for the oxygen evolution reaction. *Angew. Chem. Int. Ed.* **2016**, *128*, 5363–5367. [[CrossRef](#)]
124. Dresch, S.; Luo, F.; Schmack, R.; Kühl, S.; Gliech, M.; Strasser, P. An efficient bifunctional two-component catalyst for oxygen reduction and oxygen evolution in reversible fuel cells, electrolyzers and rechargeable air electrodes. *Energy Environ. Sci.* **2016**, *9*, 2020–2024. [[CrossRef](#)]
125. Park, S.; Shao, Y.; Liu, J.; Wang, Y. Oxygen electrocatalysts for water electrolyzers and reversible fuel cells: Status and perspective. *Energy Environ. Sci.* **2012**, *5*, 9331–9344. [[CrossRef](#)]
126. Pellow, M.A.; Emmott, C.J.M.; Barnhart, C.J.; Benson, S.M. Hydrogen or batteries for grid storage? A net energy analysis. *Energy Environ. Sci.* **2015**, *8*, 1938–1952. [[CrossRef](#)]
127. Available online: <https://fuelcellworks.com/news/reversible-protonic-ceramic-fuel-cells-able-to-store-energy/7> (accessed on 18 August 2023).
128. Putilov, L.P.; Tsidilkovski, V.I. Improving the performance of protonic ceramic fuel cells and electrolyzers: The role of acceptor impurities in oxide membranes. *Energy Convers. Manag.* **2022**, *267*, 115826. [[CrossRef](#)]
129. Kreuer, K.D. Proton-Conducting Oxides. *Annu. Rev. Mater. Res.* **2003**, *33*, 333–359. [[CrossRef](#)]
130. Kreuer, K.-D. Proton Conductivity: Materials and Applications. *Chem. Mater.* **1996**, *8*, 610–641. [[CrossRef](#)]

131. Kreuer, K.-D.; Paddison, S.J.; Spohr, E.; Schuster, M. Transport in Proton Conductors for Fuel-Cell Applications: Simulations, Elementary Reactions, and Phenomenology. *Chem. Rev.* **2004**, *104*, 4637–4678. [[CrossRef](#)]
132. Zvonareva, I.; Fu, X.-Z.; Medvedev, D.; Shao, Z. Electrochemistry and energy conversion features of protonic ceramic cells with mixed ionic-electronic electrolytes. *Energy Environ. Sci.* **2022**, *15*, 439–465. [[CrossRef](#)]

Disclaimer/Publisher’s Note: The statements, opinions and data contained in all publications are solely those of the individual author(s) and contributor(s) and not of MDPI and/or the editor(s). MDPI and/or the editor(s) disclaim responsibility for any injury to people or property resulting from any ideas, methods, instructions or products referred to in the content.